Theses, Dissertations and Capstones

1-1-2009

Structural Determination of the 5' Untranslated Regions of IRE-containing mRNAs

Chandra Sekhar Bathina
sekhar.vet@gmail.com

Recommended Citation

Structural Determination of the 5' Untranslated Regions of IRE-containing mRNAs

By

Chandra Sekhar Bathina

A thesis submitted to the

Graduate Faculty of the Department of Chemistry

At

Marshall University

In partial fulfillment of the requirements for the degree

Of

Master of Science

Dr. Bin Wang, Thesis adviser

Dr. Michael L. Norton Committee member

Dr. Leslie Frost, Committee member

Marshall University

Fall 2009

ABSTRACT

The expression of ferritin and amyloid precursor protein (APP) is post-transcriptionally regulated by iron-regulating proteins via binding to a stem-loop structure known as an iron-responsive element in the 5'-untranslated region (5'UTR) of ferritin and APP mRNAs. In this study, we used atomic force microscopy (AFM) to visualize the conformation of the 5'UTRs of ferritin heavy chain (Ferritin-H), ferritin light chain (Ferritin-L), and APP mRNA transcripts from human and mouse, and determined the secondary RNA structures using selective 2'-hydroxyl acylation analyzed by primer extension (SHAPE). The AFM imaging did not provide high resolution structural information about these RNAs, whereas the SHAPE procedure successfully interrogated the secondary RNA structures at single nucleotide resolution. To our knowledge, this is the first time that the secondary structures of the entire 5'UTRs of these RNA molecules have been experimentally mapped. This study paves the way for the further investigation of RNA-ligand interactions in these RNA molecules.

ACKNOWLEDGEMENTS

TABLE OF CONTENTS

LIST OF FIGURES

LIST OF TABLES

CHAPTER 1

Introduction

1.1. Iron storage and ferritin

Iron is an essential element required for normal cell growth and proliferation. Iron participates in the cellular processes of aerobic metabolism and enzymatic reactions, and is necessary for the synthesis of myelins, the development of neuronal dendritic trees, and the signal transduction of neurotransmitters in the brain.[1-3] For the proper function of organs, it is crucial to maintain iron homeostasis. Iron deficiency (also called hypoferremia) results in anemia, whereas iron overload (i.e., the build-up of excess iron in the body) induces hemochromatosis.[3]

The ubiquitous iron storage protein, ferritin, is responsible for both intracellular iron storage in a nontoxic state, and the controllable release of iron when necessary.[4] Mammalian ferritin forms a spherical protein cage that contains 24 subunits, each made of a 4-helix bundle (see Figure 1).[4] There are channels on the protein shell to allow iron exchange and proton transfer. The 24 subunits of the ferritin protein are composed of two functionally-distinct species encoded by two different genes. The first species, ferritin heavy chain (Ferritin-H), has an apparent molecular weight of 21,000 Da; the second, ferritin light chain (Ferritin-L), has an apparent molecular weight of 19,000 Da. The ratio of Ferritin-H to Ferritin-L in a ferritin protein varies in different tissues.[4,5]

1
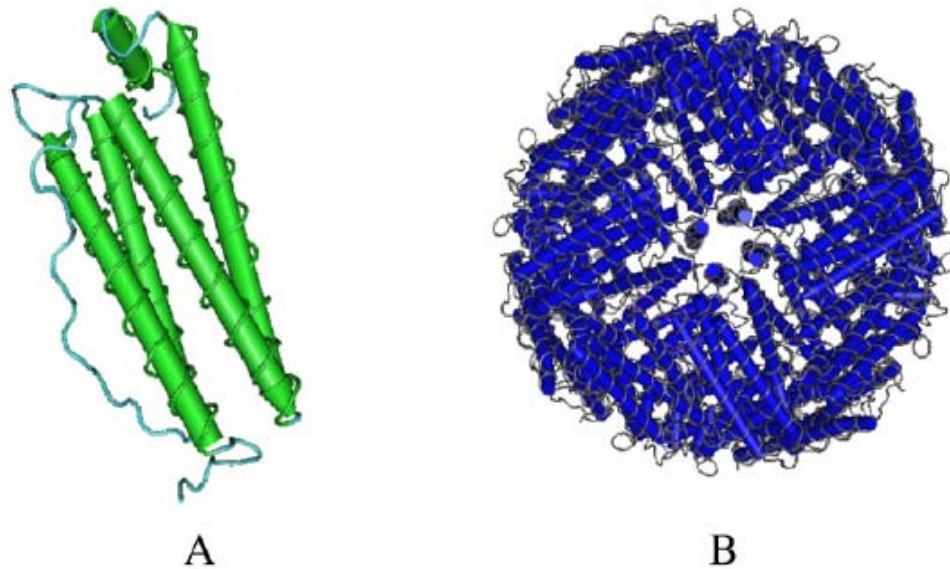
Figure 1. The structure of the mammalian ferritin protein. (A) Each subunit folds into a 4-helix bundle, and (B) the 24 subunits pack to form a spherical shell for iron storage. (Adapted, with permission, from Reference 4)

The deposition of iron into the ferritin cavity involves iron and oxygen chemistry. Ferrous ions (Fe^{2+}) react with oxygen (O_2) and/or peroxide (H_2O_2) to form a ferricoxohydroxide core, which is similar to the mineral ferrihydrite (reactions shown below). Ferritin-H catalyzes the oxidation of Fe^{2+}; whereas Ferritin-L promotes the nucleation of ferricoxohydroxide in order to store iron.[6,7]

$$2Fe^{2+} + O_2 + 4H_2O \rightarrow 2Fe(O)OH_{core} + H_2O_2 + 4H^+$$

$$2Fe^{2+} + H_2O_2 + 2H_2O \rightarrow 2Fe(O)OH_{core} + 4H^+$$
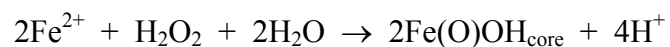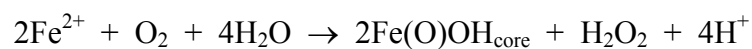
Excess free (i.e., unbound) iron is cytotoxic because it can react with reactive oxygen species such as H_2O_2 to form highly toxic hydroxyl free radicals (the Fenton chemistry reaction is shown below).[4] Free radicals can attack other stable molecules and steal their electrons. The attacked molecules then become free radicals themselves, thus setting off a chain reaction. Free radicals can damage DNA, RNA, proteins, and lipids, and cause the breakdown of cell membranes.[8,9] Therefore, the synthesis of intracellular ferritin must be regulated in order to accommodate the need to store excess iron.

$$Fe^{2+} + H_2O_2 \rightarrow Fe^{3+} + OH^- + \cdot OH \quad \text{(Fenton reaction)}$$

1.2. Iron-responsive elements in the 5'-untranslated region of ferritin mRNA

Ferritin expression is post-transcriptionally regulated by two iron-regulating proteins (IRP1 and IRP2) via binding to a stem-loop structure known as an iron-responsive element (IRE) in the 5'-untranslated region (5'UTR) of the ferritin messenger RNA (mRNA).[10-12] When the intracellular free iron content is low, IRPs specifically bind to ferritin IRE RNA, thus inhibiting ribosome binding and the corresponding ferritin translation. When the iron concentration is high, IRP-IRE binding is inhibited, thus allowing the synthesis of additional ferritin proteins for iron storage.[10]

IREs are conserved RNA motifs that contain an approximately 30-nucleotide-long sequence that forms a hairpin stem-loop structure. The apical loop of the hairpin includes a

highly conserved CAGUGN sequence, where N can be A, C, or U, but not G. Ferritin-H and

Ferritin-L mRNAs both have an IRE in their 5'UTRs.

1.3. Iron accumulation and neurodegenerative diseases

Studies have demonstrated that severe iron accumulation in the brain is correlated to

neurodegenerative disorders such as Alzheimer's disease and Parkinson's disease.[13-19]

Alzheimer's disease is the most common progressive human neurodegenerative disorder, and

is the fifth leading cause of death in adults aged 65 or older.[20] This brain disorder was first

described by German physician Alois Alzheimer in 1906.[21] People with Alzheimer's disease

undergo memory decline and thinking and behavioral changes, followed by the loss of self-

care ability.[22] There are 5.3 million Americans suffering from Alzheimer's disease, which

imposes a heavy burden on those individual's families and the health care system more

generally.[23]

One of the main physiological characteristics of Alzheimer's disease is the formation

of extraneuronal senile plaques containing aggregated amyloid β peptide (Aβ), a 40-42

amino acid product derived from the serial cleavage of the amyloid precursor protein (APP)

by β-secretase and γ-secretase.[24-29] The accumulation of Aβ interrupts synaptic transmission

and alters synaptic plasticity. APP is a large type-1 transmembrane protein that is expressed

in most cell types and is concentrated in the synapses of neurons.[25] Beta-secretase, also

known as β-site APP-cleaving enzyme 1 (BACE1), is a type-1 transmembrane protein that

has aspartyl protease activity.[30,31] BACE1 extracellularly cleaves APP at the N-terminus.[32]

The C-terminal fragment of APP, which contains 99 amino acids (C99), remains bound to the membrane. Gamma-secretase, a protein complex consisting of presenilins, nicastrin, anterior pharynx-defective phenotype-1, and PS enhancer-2, further cleaves C99 within the transmembrane domain to release an extracellular, hydrophobic Aβ peptide (see Figure 2).[24,26,28] It has been discovered that the deposition of Aβ in the brain is largely due to increased APP/BACE1 expression and activity.[33-37] In addition, increased oxidative stress due to misregulated iron homeostasis also plays an important role in the pathogenesis of Alzheimer's disease.[38-40] Elevated iron concentrations have been detected in hippocampus, basal nucleus of meynert, senile plaques, and neurofibrillary tangles in the brain of Alzheimer's patients.[41,42]
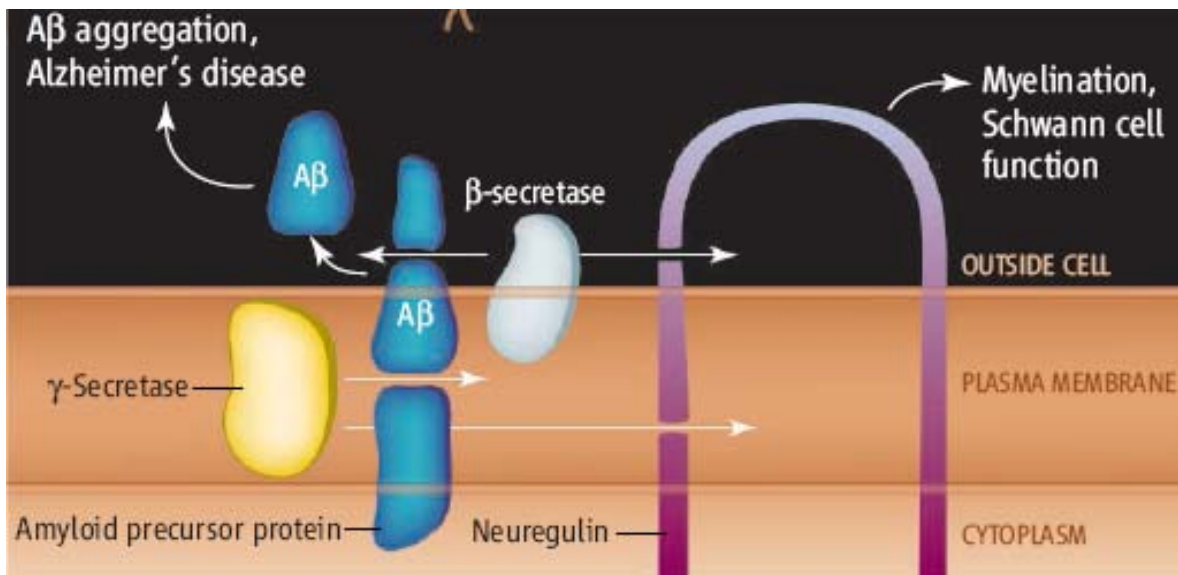
Figure 2. An overview of the cleavage of APP by β-secretase and γ-secretase. (Adapted, with permission, from Reference 24)

Parkinson's disease is the second most common human neurodegenerative disorder, with symptoms that include resting tremors, difficulty balancing, moving and talking, stiffness of limbs, and dementia.[43] The etiology of Parkinson's disease remains unclear. However, several factors play pivotal roles, including the elevated expression level of the presynaptic protein α-synuclein (SNCA), and the elevated iron concentration.[13,14,44-50] The aggregated SNCA is the main component of Lewy bodies, abnormal protein clusters found in the brains of Parkinson's patients. SNCA duplication and triplication as well as genetic variability in the promoter and 3' untranslated region (3'UTR) have been reported to associate with familial Parkinson's disease.[44-46,48,51] Elevated iron concentrations in the substantia nigra pars compacta have been implicated in the development of idiopathic Parkinson's disease.[52,53]

An individual ferritin molecule can bind up to 4500 iron atoms.[4] However, ferritin in the substantia nigra of Parkinson's patients was reported to contain more iron than ferritin in the substantia nigra of healthy people.[54] The overloaded ferritin was still unable to take up enough iron to properly regulate iron levels in the brains of Parkinson's patients. Furthermore, research shows that the ferritin level in Parkinson's patients was independent of iron level, i.e., the increased iron content observed in the brains of Parkinson's patients was not accompanied by an increased ferritin level.[54] The absence of ferritin up-regulation might be due to the increased binding activity of IRP to the IRE of ferritin RNA in the presence of nitric oxide. Other mechanisms may also be involved.[54]

1.4. IRE in the 5'UTRs of APP and SNCA mRNAs

In 2002, an IRE-type structure was found in the 5'UTR of the APP mRNA.[55] In 2007, an IRE-like stem-loop structure was found in the 5'UTR of the SNCA mRNA.[56,57] These IRE-type sequences interact with IRPs to control the corresponding protein synthesis.[57,58] The mechanism is similar to that of the iron-dependent translational regulation of Ferritin-H and Ferritin-L synthesis via IREs in their 5'UTRs. Tens of thousands of compounds have been screened to identify ligands that can bind to the 5'UTR of the human APP mRNA, which would allow the treatment of Alzheimer's disease by decreasing the production of APP and the corresponding Aβ; fifteen compounds were identified as inhibiting APP translation by interacting with the 5'UTR of APP mRNA.[59-66] The fifteen molecules are: iron chelators desferrioxamine (DFO), iodochlorhydroxyquin (clioquinol), M30, HLA20, and VK28 (varinel), copper chelator tetrathiomolybdate, lead and mercury chelator dimercaptopropanol, naturally occurring iron and copper chelators (-)-epigallocatechin-3-gallate (EGCG) and curcumin, bi-functional metal chelator XH-I, macrolide antibiotics Azithromycin and Erythromycin, selective serotonin reuptake inhibitor and chelator Paroxetine, anticholinesterase Phenserine, and antioxidant N-acetyl cysteine.

Some of the molecules mentioned above showed clinical effectiveness in slowing AD dementia.[61,64,65] However, the underlying mechanism(s) has not been determined. For example, what conformation does APP mRNA 5'UTR adopt after the binding of a small molecule? Which nucleotides do the ligands bind to in the IRE? Do the ligands also bind to other regions in the 5'UTR of APP mRNA, such as the interleukin-1 responsive acute box?

If the molecules mentioned above have the capability to reduce APP expression, can they bind to the IRE in human SNCA mRNA 5'UTR to inhibit SNCA synthesis? Do they have the capability to inhibit Ferrtin-H and Ferritin-L translation as well? It is an advantage if these molecules can down-regulate APP and SNCA expression, but certainly a disadvantage if they down-regulate the expression of ferritin.

1.5. Objective of the study

In order to substantially improve the understanding of ligand-RNA binding mechanisms and to shed light on the design of novel molecules targeted to specific RNA motifs, a complete elucidation of the RNA conformation before, during, and after ligand binding is necessary. The objective of this study is to determine the conformations of the 5'UTRs of human and mouse Ferritin-H, Ferritin-L, and APP mRNA transcripts in the absence of the ligand. The long-term goal of this study is to speed up the discovery of potential therapeutic agents for the treatment of neurodegenerative diseases.

1.6. Techniques used in the study

1.6.1. Atomic force microscopy

For this project, two cutting-edge technologies were used to study the structural characteristics of RNA. First, atomic force microscopy (AFM) was applied to visualize the conformation of RNA transcripts. AFM was invented in 1986, and the technique soon

became a potent tool for biological research.[67-70] The principle of AFM is based on the mechanical interaction that occurs between a sample surface and a cantilevered sharp silicon tip (5-10 nm radius at the point of the tip), when a small, constant force is applied. A piezoelectric tube scanner is used to scan the tip over the sample surface. The tip-sample interaction is detected by monitoring the deflection of the cantilever using a photodiode detector (see Figure 3).[67] AFM enables the study of the three-dimensional topography of a sample surface with a resolution at the Angstrom level. The simple sample preparation procedure for AFM imaging makes it much more convenient than conventional imaging techniques such as X-ray crystallography and electron microscopy.

AFM can be operated both in air and in a liquid solution, and no sample coating or staining is required; therefore, the conformation of biological macromolecules (e.g., DNA, RNA, and proteins) adsorbed onto a smooth mica surface can be visualized under quasi-native (i.e., close to physiological) conditions.[71-74] Jaeger's research group has recently used AFM to visualize the static RNA nanoarchitectures they designed, including tectoRNA and kissing-loop RNA.[75] Samori's research group applied AFM to study the secondary structure of Turnip Yellow Mosaic Virus RNA.[76] Gamarnik and colleagues used AFM to investigate the long-range RNA interactions that circularize the 5'- and 3'-end of the dengue virus.[77]
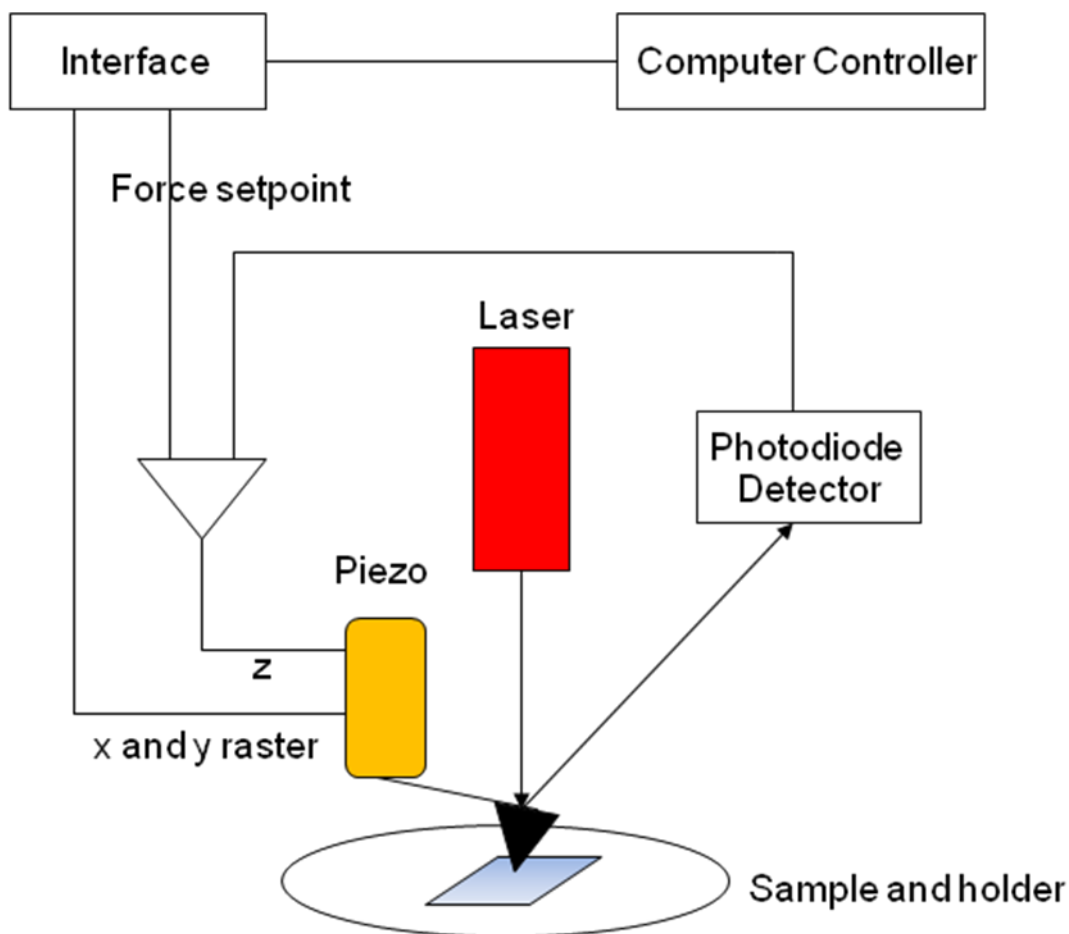
Figure 3. A schematic diagram of AFM.

1.6.2. Selective 2'-hydroxyl acylation analyzed by primer extension

In addition to AFM visualization, the SHAPE (Selective 2'-Hydroxyl Acylation analyzed by Primer Extension) technique was used to determine RNA secondary structures. Invented in 2005, the theoretical basis of SHAPE chemistry is that the local nucleotide flexibility of an RNA can be monitored by treating the RNA with 2'-hydroxyl-reactive electrohphiles such as *N*-methylisatoic anhydride (NMIA) or 1-methyl-7-nitroisatoic anhydride (1M7), which selectively and covalently modify flexible nucleotides (i.e., single-

stranded RNA nucleotides) at the 2'-ribose position.[78-80] Treating RNA with the NMIA/1M7

reagent (usually $\leq$ 10 mM) results in modifications approximately once in every several

hundred nucleotides. The detection of the modified RNA nucleotides is based on primer

extension to convert RNA to its complementary DNA (cDNA) by reverse transcriptase. The

presence of a 2'-*O*-adduct causes the reverse transcription to stop exactly one nucleotide

prior to the modified position, whereas RNA without NMIA/1M7 treatment produces a full-

length cDNA.[78] The amplified cDNA fragments are analyzed by conventional slab gel

electrophoresis (for radio-labeled DNA fragments) or capillary gel electrophoresis (for

fluorescently-labeled DNA fragments) to provide RNA structural information.[81,82]

Compared to traditional RNA structure-mapping techniques such as enzymatic cleavage and

chemical modification, which are time consuming and evaluate only a subset of nucleotides

in an RNA, SHAPE chemistry is a rapid, high-throughput technology with single nucleotide

resolution.

Figure 4 shows an example of SHAPE data obtained from capillary gel

electrophoresis. The SHAPE reactivity of each nucleotide of yeast tRNA[Asp] can be

determined by subtracting the control peak area from the NMIA peak area and the

subsequent normalization. Peaks with high amplitudes correspond to the conformationally

flexible (i.e., single-stranded) nucleotides, whereas peaks with low amplitudes correspond to

the conformationally-constrained (i.e., base-paired or tertiary interaction-involved) positions.

SHAPE data are applicable to constrain RNA structural prediction algorithms and can

dramatically improve the predication accuracy of the RNA secondary structures.
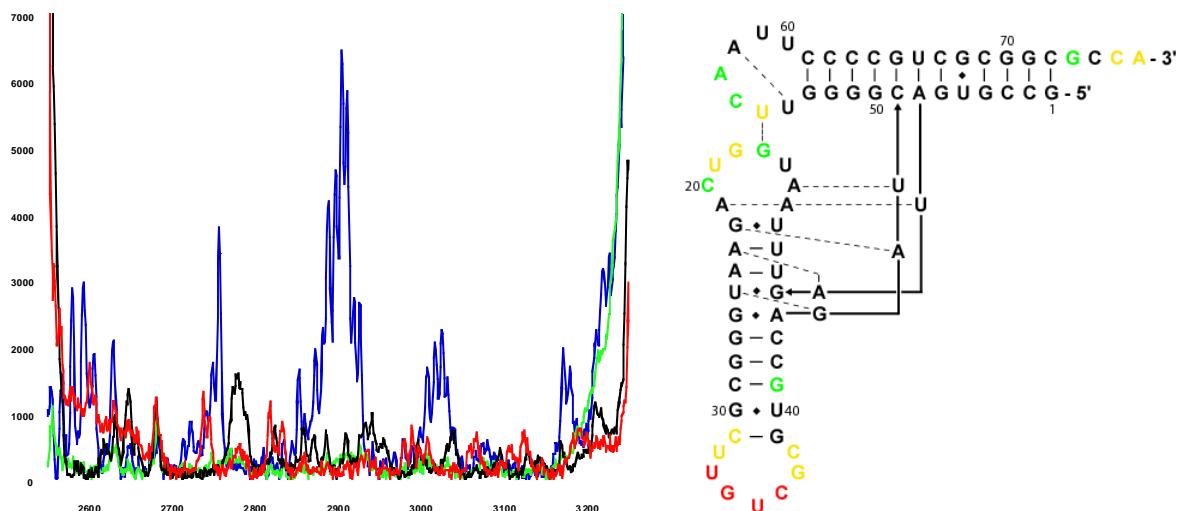
Figure 4. An example of SHAPE data obtained from capillary gel electrophoresis. Left: SHAPE raw data from *Saccharomyces cerevisiae* tRNA[Asp] transcript obtained by capillary gel electrophoresis. The blue trace is +NMIA sample; the green trace is -NMIA negative control; black and red traces are two dideoxy ladders (ddC and ddT, respectively). The x-axis indicates the number of data points collected. The y-axis enumerates the fluorescence units. Right: Individual nucleotide reactivity based on SHAPE data. Red-coded nucleotides correspond to 60-100% of SHAPE reactivity; yellow-coded nucleotides correspond to 25-60% of SHAPE reactivity; green-coded nucleotides correspond to 10-25% of SHAPE reactivity; black-coded nucleotides correspond to 0-10% of SHAPE reactivity.

Figure 5 shows an example of the use of SHAPE chemistry coupled with an autoradiography/slab gel electrophoresis detection system to study magnesium-induced conformational changes in yeast tRNA[Asp].[81] Wang and colleagues used 1M7 instead of NMIA to run SHAPE experiments because the reactivity of 1M7 is not significantly modulated by ions in solution. As expected, SHAPE reactivity exactly recapitulates the native structure of tRNA[Asp]. Wang *et al.* explored Mg^{2+}-dependent structural changes over a

wide range of ion concentrations (20 to 0 mM, Figure 5A, 19 left-most lanes). Smooth

transitions for almost every nucleotide in tRNA^{Asp} were observed. A well-defined model for

the final non-native state was developed based on the SHAPE reactivity information (Figure

5C). Removing Mg^{2+} destabilizes tertiary interactions in the variable loop and thereby

allows this region to form stable, non-native base pairs with nucleotides in the D-loop.[81]
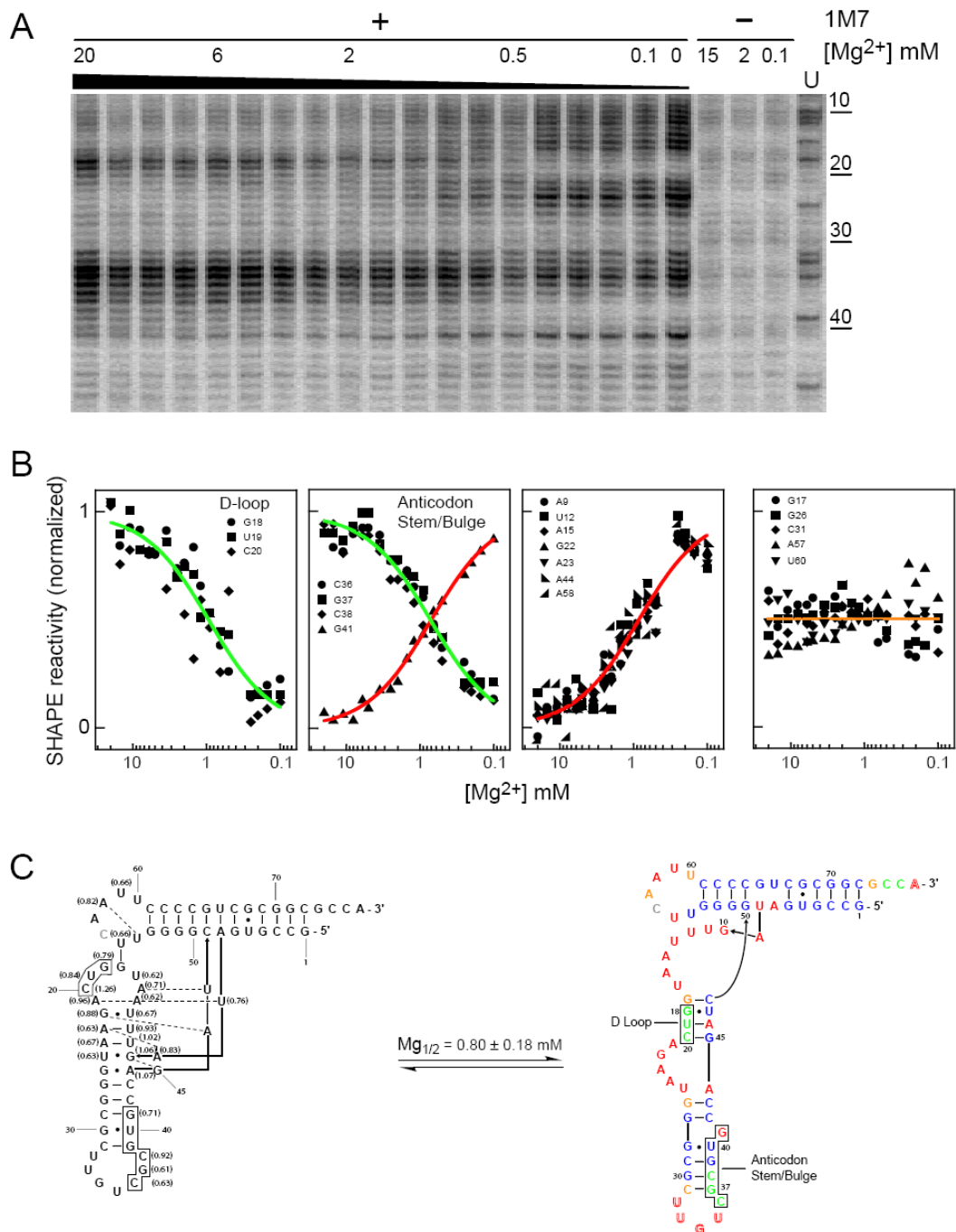
Figure 5. Mg^{2+}-dependent unfolding of $tRNA^{Asp}$. (A) $tRNA^{Asp}$ modification upon removing Mg^{2+} as visualized by RNA SHAPE chemistry. Experiments were performed as a function of [$MgCl_2$] in the presence (+) and absence (−) of 1M7 reagent. (B) Mg^{2+}-induced

structural transitions, illustrated for instructive nucleotide positions. (C) Structural model for the unfolding of tRNA^{Asp} in the absence of Mg^{2+}. $Mg_{1/2}$ values are listed for nucleotides that show greater than a two-fold reactivity change over the titration. Nucleotides exhibiting 2-fold or larger changes in reactivity as compared to the native state are colored red (increase) and green (decrease); nucleotides showing <2-fold changes are colored blue (unreactive, SHAPE reactivity ≤0.3), orange (moderately reactive, 0.3< SHAPEreactivity <0.7), and red outline (highly reactive, SHAPE reactivity ≥0.7). (Adapted, with permission, from Reference 81)

In this study, we used AFM to visualize the conformation of the 5'UTRs of Ferritin-H, Ferritin-L, and APP mRNA transcripts from two species (human and mouse), and determined the secondary RNA structures using SHAPE analysis coupled with a fluorescence detection system. To our knowledge, this is the first time that the secondary structures of the 5'UTRs of APP mRNA in human and mouse have been experimentally mapped. This study paves the way for the further investigation of RNA-ligand interactions in these RNA molecules.

CHAPTER 2

Experimental Methods

2.1. DNA

DNA of human Ferritin-H 5'UTR: The 200-nucleotide-long DNA template (5'-ACAAGCGACCCGCAGGGCCAGACGTTCTTCGCCGAGAGTCGTCGGGGTTTCCTG CTTCAACAGTGCTTGGACGGAACCCGGCGCTCGTTCCCCACCCCGGCCGGCCGCC CATAGCCAGCCCTCCGTCACCTCTTCACCGCACCCTCGGACTGCCCCAAGGCCCC CGCCGCCGCTCCAGCGCCGCGCAGCCACCGCCGCCG-3'), forward primer that included a T7 promoter sequence (5'-TAATACGACTCACTATAGGATAAGAGACCACAAGCGACCCGCAGGGCCAG-3'), and reverse primer (5'-GGCGGCGACTAAGGAGAGGCGGCGGCGGCGGCGGTGGCTGCGCGGCGCTG-3') were obtained from Integrated DNA Technologies, Inc. (IDT, San Diego, CA) and were used to amplify the 254-base pair Ferritin-H 5'UTR. The Polymerase Chain Reaction (PCR) mixture (1.0 ml total volume) contained 20 mM Tris (pH 8.4), 10% dimethyl sulfoxide (DMSO), 50 mM KCl, 2.5 mM $MgCl_2$, 0.2 mM of each dNTP (dATP, dGTP, dCTP, and dTTP), 0.5 μM each of forward and reverse primer, 5 pM of DNA template, and 0.025 U/μl Taq DNA polymerase. The PCR product was inspected by ethidium bromide-stained agarose gel electrophoresis and purified by ethanol precipitation.

DNA of human Ferritin-H short 5'UTR: To obtain a PCR ready cDNA, Human

Brain Total RNA (Ambion, Austin, TX) was reverse-transcribed using a high capacity cDNA

reverse transcription kit from Applied Biosystems (Foster City, CA). A 224-base pair

segment of DNA that encodes the Ferritin-H short 5'UTR was amplified using the resultant

cDNA as a template, along with a forward primer containing the T7 promoter (5'-

TAATACGACTCACTATAGGATAAGAGACCACAAGCGACCCG-3') and reverse

primer (5'-GCGGTGGCTGCGCGGCGCTGGAG-3'), both of which were synthesized at

IDT. The PCR reaction was performed using 0.2 mL, but was otherwise as described above.

The product was inspected by ethidium bromide-stained agarose gel electrophoresis and

purified using the QIAquick PCR purification kit (Qiagen, Valencia, CA).

DNA of human Ferritin-L 5'UTR: FirstChoice[®] PCR-ready Human Brain cDNA

(Ambion, Austin, TX) (2 ng) was used as a template to amplify the 234 base-pair Human

Ferritin-L 5'UTR. Both the forward primer, which contained a T7 promoter sequence (5'-

TAATACGACTCACTATAGGGCAGTTCGGCGGTCCCGCGGGTCTGTCTCT-3'), and

the reverse primer (5'-GAATCTGGGAGCTCATGGTTGGTTGGC-3') were synthesized at

IDT. A 0.2 ml PCR reaction was performed as described above. The product was inspected

by ethidium bromide-stained agarose gel electrophoresis and purified using the QIAquick

PCR purification kit (Qiagen, Valencia, CA).

DNA of human APP 5'UTR: FirstChoice[®] PCR-ready Human Brain cDNA (Ambion,

Austin, TX) (2 ng) was used as a template to amplify the 180-base pair human APP 5'UTR.

Both the forward primer, which contained a T7 promoter sequence (5'-

TAATACGACTCACTATAGGAGTTTCCTCGGCAGCGGTAGGCGAG-3'), and the reverse primer (5'-AAACCGGGCAGCATCGCGACC-3') were obtained from IDT. A 0.2 ml PCR was performed as described above. The product was inspected by ethidium bromide-stained agarose gel electrophoresis and purified using the QIAquick PCR purification kit (Qiagen, Valencia, CA).

DNA of mouse Ferritin-H 5'UTR: FirstChoice® PCR-ready Mouse Brain cDNA (Ambion, Austin, TX) (2 ng) was used as a template to amplify the 186-base pair mouse Ferritin-H 5'UTR. Both the forward primer, which contained a T7 promoter sequence (5'-TAATACGACTCACTATAGGCAGACGTTCTCGCCCAGAGTCGCC-3'), and the reverse primer (5'-GGTGGCGGCGGGGCGAGGCGCGGT-3') were obtained from IDT. A 0.2 ml PCR reaction was performed as described above. The product was inspected by ethidium bromide-stained agarose gel electrophoresis and purified using the QIAquick PCR purification kit (Qiagen, Valencia, CA).

DNA of mouse Ferritin-L 5'UTR: Mouse Brain Total RNA (Ambion, Austin, TX) was reverse-transcribed using a high capacity cDNA reverse transcription kit from Applied Biosystems (Foster City, CA). The resultant cDNA product was used as a template to amplify the 224-base pair mouse Ferritin-L 5'UTR. Both the forward primer (5'-TAATACGACTCACTATAGAGCAGCGCCTTGGAGGTCCCGTG-3') and reverse primer (5'-GGCTGATCCGGAGTAGGAGCTAAC-3') were obtained from IDT. A 0.2 ml PCR reaction was performed as described above. The product was inspected by ethidium

18

bromide-stained agarose gel electrophoresis and purified using the QIAquick PCR purification kit (Qiagen, Valencia, CA).

DNA of mouse APP 5'UTR: The reverse-transcribed mouse brain cDNA product described above was used as a template to amplify the 164-base pair mouse APP 5'UTR. Both the forward primer (5'-TAATACGACTCACTATAGGGTTTCCTCGGCGGCGGGAGGCGAGA-3') and reverse primer (5'-CGTGATCCTGCGTGGGCCACCGAGT-3') were synthesized at IDT. A 0.2 ml PCR reaction was performed as described above. The product was inspected by ethidium bromide-stained agarose gel electrophoresis and purified using the QIAquick PCR purification kit (Qiagen, Valencia, CA).

2.2. RNA

RNA from the human Ferritin-H 5'UTR was transcribed from 1.0 ml of a solution containing 50 µg of PCR-generated DNA, 40 mM Tris (pH 7.8), 20 mM NaCl, 6 mM $MgCl_2$, 2 mM spermindine HCl, 10 mM DTT, 1 mM of each NTP (ATP, GTP, CTP, and UTP), 0.1 U/µl SUPERaseIn[TM] RNase inhibitor, and 2 U/µl T7 RNA polymerase; incubation was at 37 °C for 4-5 hours. RNA transcripts were treated with TURBO[TM]DNase (Ambion, Austin, TX) to destroy any remaining DNA. The DNase was then deactivated by adding ethylenediaminetetraacetic acid (EDTA) to a final concentration of 15 mM, followed by heating at 75 °C for 15 minutes. The RNA transcripts were concentrated by ethanol precipitation, purified by 8% polyacrylamide gel electrophoresis (PAGE), and recovered by

passive elution overnight at 4 °C in a solution containing 0.5 M sodium acetate and 1 mM EDTA.

RNAs from the human Ferritin-H short 5'UTR, human Ferritin-L 5'UTR, human APP 5'UTR, mouse Ferritin-H 5'UTR, mouse Ferritin-L 5'UTR, and mouse APP 5'UTR were transcribed from 0.2 ml of a solution having the same composition as described above, except that only 5 µg of the PCR-generated DNA was used here. The RNA transcripts were purified using a MEGAclear^{TM} Kit (Ambion, Austin, TX) instead of PAGE due to the relatively low yields. The purity and integrity of the seven RNA samples were tested by running a RNA 6000 nano-chip on an Agilent 2100 Bioanalyzer (Agilent, Santa Clara, CA).

2.3. AFM

A 3.5 µl aliquot of an approximately 1 µM RNA sample in TE buffer (10 mM Tris at pH 8.0 and 1 mM EDTA at pH 8.0) was combined with 1.5 µl of folding buffer (final concentration, 100 mM Tris-HCl at pH 8.0, 100 mM NaCl, and 6 mM $MgCl_2$) and incubated at 37 °C for 20-30 minutes. The 5.0 µl of solution was deposited on freshly cleaved mica, and the RNA was allowed to adsorb to the mica surface for 5 minutes. The non-adsorbed RNA was removed from the mica surface by washing with nuclease-free water, after which the sample was dried with a stream of nitrogen. All images were collected in air using a Thermomicroscopes Explorer AFM (Veeco, CA) with a Tube or Tripod scanner. Images were obtained while using either Micromash DP15/HiRes-W/AIBS tips (nominal radius of tip curvature ≈ 1 nm, Al reflective side coating, cantilever length = 230 µm, width = 35 µm,

20

resonant frequency = 325 kHz) or NSC15/AIBS tips (nominal radius of tip curvature < 10 nm, Al reflective side coating, cantilever length = 125 μm, width = 35 μm, resonant frequency = 325 kHz). Thermomicroscopes Scanning Probe Microscopy Lab Analysis software was then used to process and analyze the images for leveling and topography measurements.

2.4. SHAPE

SHAPE includes three major procedures: chemical modification of flexible RNA nucleotides, reverse transcription to identify modified RNA nucleotides, and finally data analysis and the construction of a model of the RNA secondary structure. The 8 detailed steps of SHAPE are itemized below.

1) Folding: The RNA was heated at 95°C for 2 minutes, and then cooled on ice to eliminate multimeric forms. The RNA began in 0.5× TE buffer (pH 8.0), folding buffer (final concentration, 100 mM Tris-HCl at pH 8.0, 100mM NaCl, and 6 mM $MgCl_2$) was added to the RNA solution. This new solution was incubated at 37°C for 20 minutes. After incubation, half of the solution was transferred into a second tube.

2) 1M7 modification: 1M7 in DMSO was added to the RNA solution (the first tube) at a final concentration of 6 mM, and the solution was allowed to continue incubating for 2 minutes (greater than five 1M7 half-lives). A control experiment was run in parallel where 1M7 was omitted and only DMSO was added (the second tube).

3) An ethanol precipitation was then conducted to recover RNA.

4) Primer Extension: A different color-coded fluorophore-labeled DNA primer (human Ferritin-H 5'UTR primer: 5'-GACTAAGGAGAGG-3'; human Ferritin-H short 5'UTR primer: 5'-GCGGTGGCTGCGCGGCGCTGGAG-3'; human Ferritin-L 5'UTR primer: 5'-GAATCTGGGAGCTCATGGTT-3'; human APP 5'UTR primer: 5'-AAACCGGGCAGCATCGCGAC-3'; mouse Ferritin-H 5'UTR primer: 5'-GGTGGCGGCGGGGCGAGG-3'; mouse Ferritin-L 5'UTR primer: 5'-GGCTGATCCGGAGTAGGAGCTAAC-3'; and mouse APP 5'UTR primer: 5'-CGTGATCCTGCGTGGGCCA-3') was added to the (+) 1M7 and (-) 1M7 reactions. The two samples were incubated at 65°C for 6-10 minutes followed by 35°C for 15 minutes to allow primer annealing to the 3' end of the RNA. Reverse transcription buffer (including final concentrations of 50 mM Tris-HCl at pH 8.3, 75 mM KCl, 3mM $MgCl_2$, 5 mM DTT, 0.5 mM dATP, 0.5 mM dCTP, 0.5 mM dGTP, and 0.5 mM dTTP) was added and heated to 52°C, then reverse transcriptase (Superscript III, Invitrogen, Carlsbad, CA) was added to the solution and allowed to incubate at 52°C for 15 minutes for primer extension. Two dideoxy sequencing reactions were run in parallel in order to identify peaks in the (+) and (-) 1M7 reactions.

5) Recovery of cDNA: Ethanol precipitation was used to recover cDNA, which was then resuspended in highly deionized formamide.

6) cDNA fragment analysis: The suspended cDNA was loaded onto the Applied Biosystems 310 Genetic Analyzer (ABI 310, Applied Biosystems, Foster City, CA). This system uses capillary gel electrophoresis coupled with a fluorescence detection system to determine the size of the cDNA fragments.

7) SHAPE data analysis: Data collected from ABI 310 underwent baseline adjustment, matrixing to remove signal overlap, and mobility shift adjustment using ShapeFinder software.[83] Integrated SHAPE reactivity at each nucleotide position was normalized to a scale from 0 to ~2.

8) Model Construction: The normalized SHAPE reactivities were incorporated into RNAstructure 4.6 software, which uses both nearest-neighbor free energy parameters and SHAPE data as pseudo-energy parameters to develop a secondary structure prediction.[84]

CHAPTER 3

Results

3.1. The 5'UTR of human Ferritin-H mRNA

The sequence of the 237-nucleotide-long human Ferritin-H mRNA 5'UTR is as

follows:

5'-GG AUAAGAGACC ACAAGCGACC CGCAGGGCCA GACGUUCUUC

GCCGAGAGUC GUCGGGGUUU CCUGCUUCAA CAGUGCUUGG ACGGAACCCG

GCGCUCGUUC CCCACCCCGG CCGGCCGCCC AUAGCCAGCC CUCCGUCACC

UCUUCACCGC ACCCUCGGAC UGCCCCAAGG CCCCCGCCGC CGCUCCAGCG

CCGCGCAGCC ACCGCCGCCG CCGCCGCCUC UCCUUAGUCG CCGCC-3'

3.1.1. AFM images

An AFM image of the negative control is shown in Figure 6. The negative control

was made by depositing 3.5 µl of TE buffer and 1.5 µl of folding buffer (see Experimental

Methods), without RNA, onto freshly cleaved mica and allowing it to sit for 5 minutes,

followed by washing with nuclease-free water, and drying with a stream of nitrogen. Figure

6A shows a two-dimensional image of the mica surface; Figure 6B is a three-dimensional

view of the sample surface. The surface of the sample composed of mica with the negative

control solution deposited onto it is almost featureless, with no apparent blobs. The surface

roughness is similar to that of the original mica surface.

A
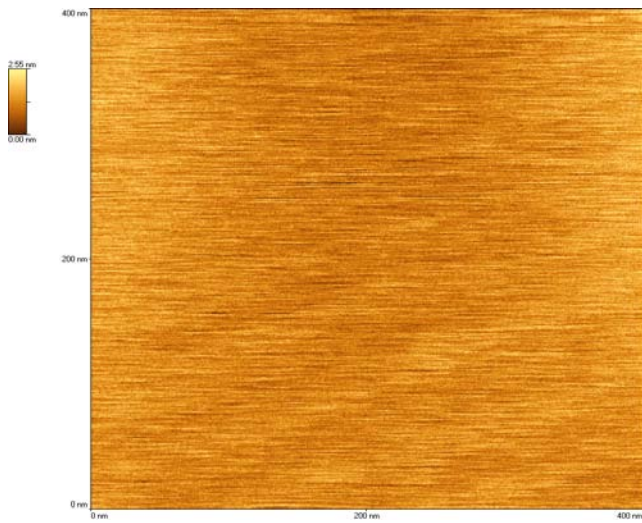
B
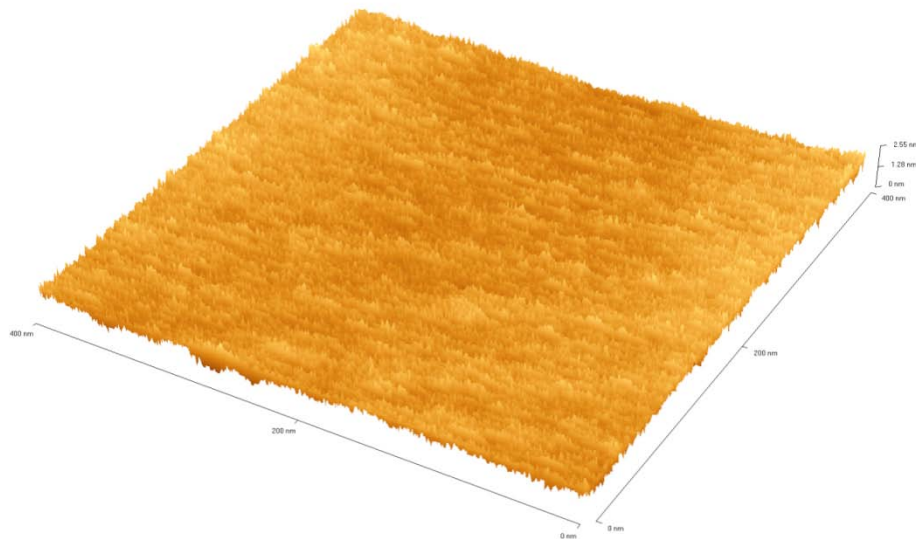
Figure 6. AFM i mages of t he mica surf ace w ith the negative co ntrol solution
deposited onto it. (A) The two-dimensional view of the sample surface, and (B) the three-
dimensional view of the sample surface.

An AFM image of a sample composed of human Ferritin-H mRNA 5'UTR deposited onto a mica surface is shown is Figure 7. The 237-nucleotide-long RNA molecule folds into a complex three-dimensional structure that appears as a blob on the mica surface. The heights of three blobs were measured using the "line analysis" tool in the Thermomicroscopes Scanning Probe Microscopy Lab Analysis software, with the maximum height of a blob recorded as its height (see Figure 8A). The heights of the eleven blobs were measured as: 0.81 nm, 0.55 nm, 0.35 nm, 0.38 nm, 0.31 nm, 0.21 nm, 0.33 nm, 0.22 nm, 0.23 nm, 0.13 nm, and 0.12 nm (average $\pm$ standard deviation = 0.33 $\pm$ 0.20 nm).

The volume of a blob was determined by drawing four lines on the blob (see Figure 8B, where only three lines are demonstrated), where line 1 was drawn parallel to the AFM tip's scanning direction (horizontal blue line); line 2 was drawn at an angle that is 135 degrees clockwise to line 1 (green line); line 3 was drawn at an angle that is 90 degrees to line 2 (red line); and line 4 was drawn at 90 degrees to line 1 and 45 degrees to lines 2 and 3 (vertical line, not shown). The length of each line was measured at half the maximum height of the blob (see Figure 8C), a measurement called Full Width at Half Maximum (FWHM). The line with the maximum FWHM value is identified as the Major Axis, and the line with minimum FWHM value is identified as the Minor Axis. The blob was then treated as an ellipsoid, and the volume was determined using the formula: Volume = 4/3 π $\times$ FWHM$_{\text{Major Axis}}$ $\times$ FWHM$_{\text{Minor Axis}}$ $\times$ Height of the blob. The volumes of the eleven blobs were 1235 nm^3, 823 nm^3, 433 nm^3, 313 nm^3, 220 nm^3, 103 nm^3, 277 nm^3, 112 nm^3, 173 nm^3, 97.0 nm^3, and 131 nm^3, respectively (average $\pm$ standard deviation = 356 $\pm$ 360 nm^3). There are several

possible explanations for the differences in height and volume of the blobs, such as 1) some blobs on the mica surface were RNA aggregates; 2) some blobs were degraded RNA molecules; and 3) RNA molecules adopted different conformations on the mica surface.

A
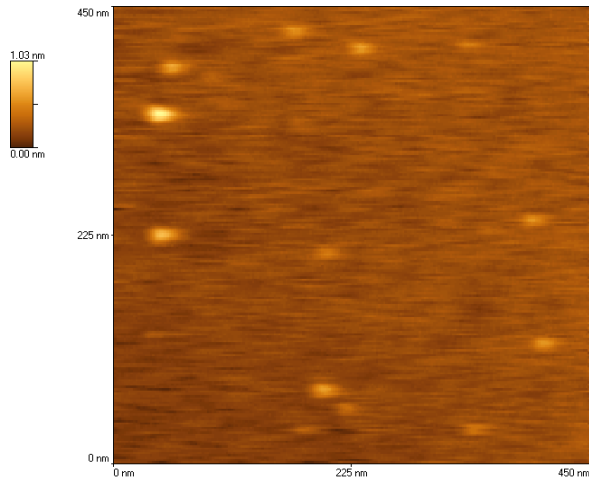
B
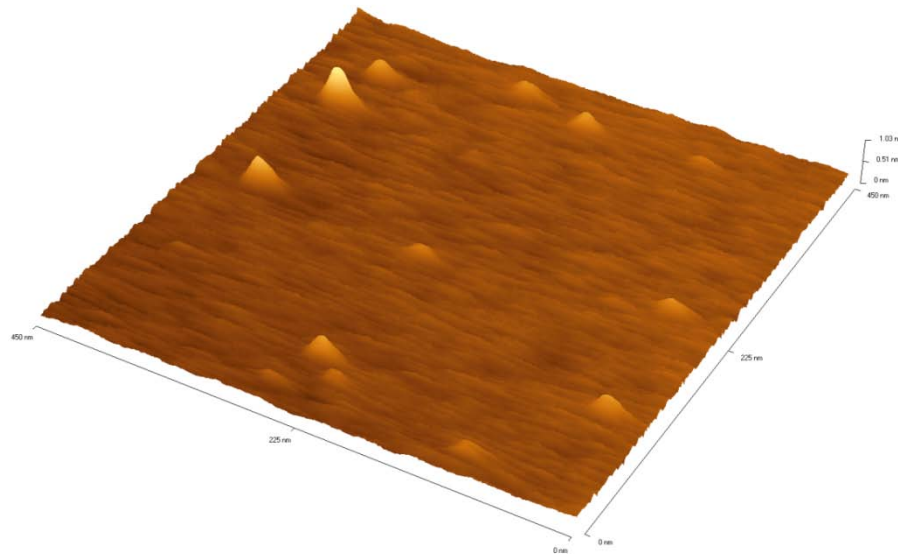
Figure 7. AFM i mages of a s ample com posed of t he h uman Ferritin-H m RNA 5'UTR deposited onto a mica surface. (A) The two-dimensional view of the sample surface, and (B) the three-dimensional view of the sample surface.

A
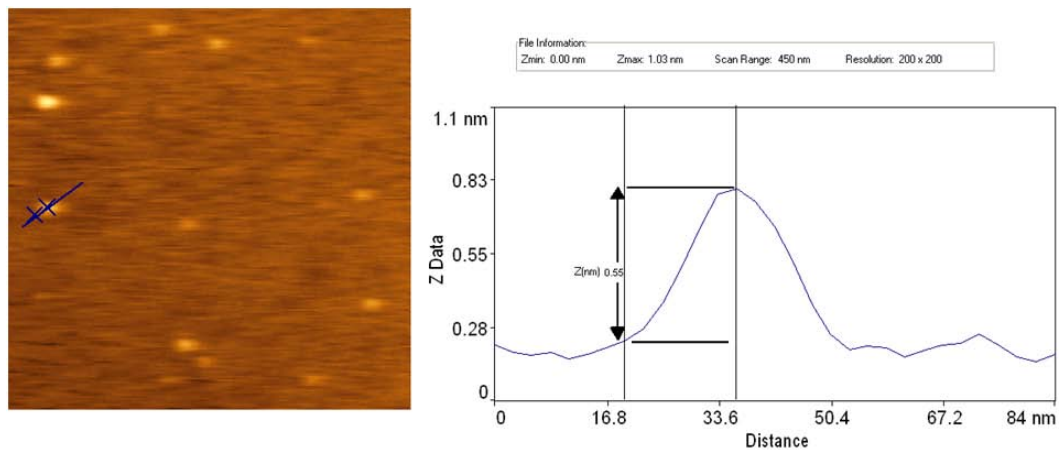
B
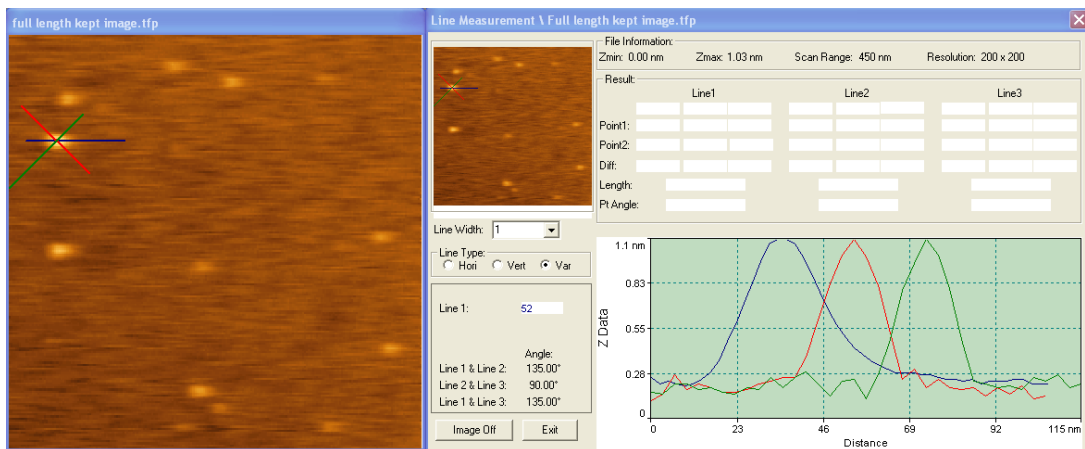
C
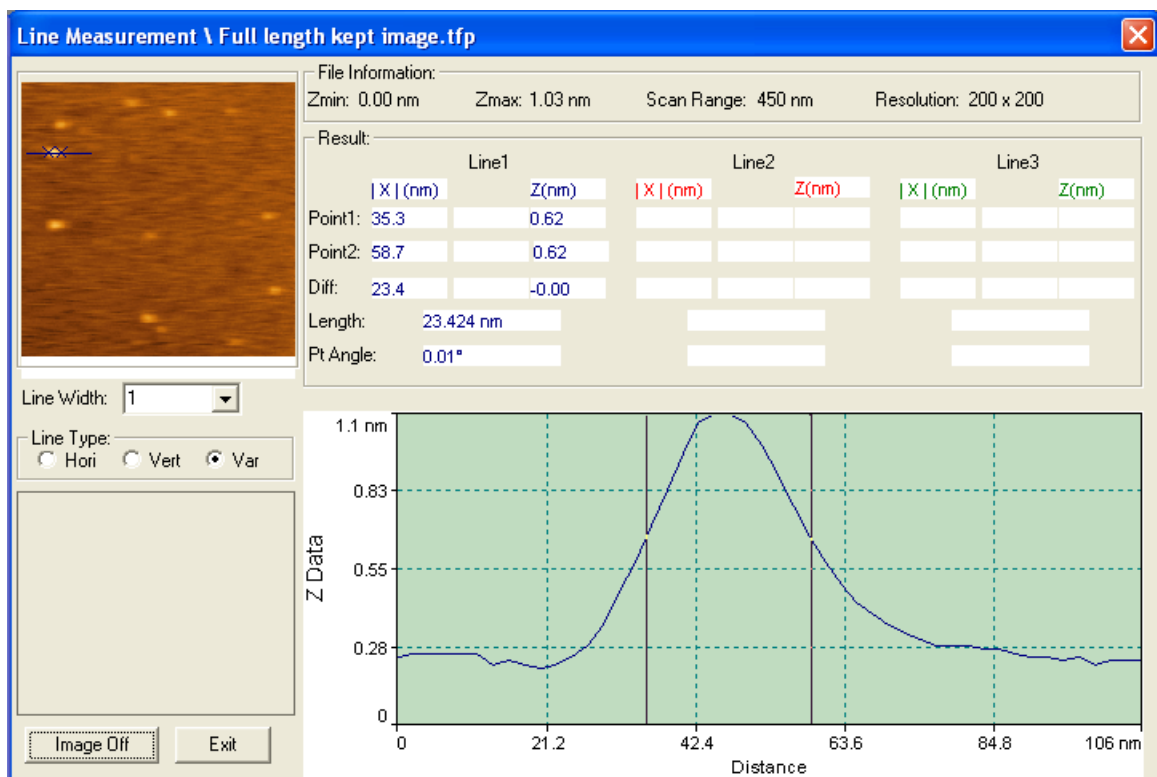
Figure 8. Illustration of line analysis from the AFM image of the human Ferritin-H mRNA 5' UTR. (A) Illustration of t he he ight m easurement of a n R NA bl ob, (B) determination of the Major Axis and the Minor Axis for an RNA blob at half the maximum height, and (C) illustration of how to measure the full width of a blob at half the maximum height (FWHM).

3.1.2. SHAPE data

The human Ferritin-H mRNA 5'UTR transcripts were folded in a solution containing 6 mM Mg^{2+} and subjected to the SHAPE procedure. The SHAPE experiments were repeated at least twice. The raw data from the ABI genetic analyzer underwent a series of

modifications in order to remove signal overlap and migration differences due to the cDNA fragments being labeled with different colored fluorophores. Figure 9 illustrates one set of SHAPE electropherograms for the human Ferritin-H mRNA 5'UTR.

After alignment and integration to obtain the Gaussian-fitted peak area at each nucleotide position for both the (+) 1M7 and (-) 1M7 traces, the background (-) 1M7 peak area was subtracted from the corresponding (+) 1M7 peak area. The absolute SHAPE reactivities obtained were normalized by excluding the 2% most reactive fluorescent intensities, and then dividing by the average of the remaining 8% most highly reactive positions. The normalized SHAPE reactivities were classified into three categories. Nucleotides with high SHAPE reactivities (≥ 0.7) are expected to be single-stranded; nucleotides with low SHAPE reactivities (<0.3) are unreactive, and are expected to be base-paired; and nucleotides with intermediate SHAPE reactivities (between 0.3 and 0.7) are difficult to judge. Nucleotides in this last category may be single-stranded or could be involved in base-pairing/tertiary interactions. Figure 10 presents the averaged SHAPE reactivities from two sets of SHAPE data for the human Ferritin-H mRNA 5'UTR.

Normalized SHAPE reactivity values (0 to ~2) were incorporated into the RNAstructure program as a pseudo free energy change term, so as to constrain the prediction of the secondary structure of the RNA. The predicted structure with the lowest free energy for the human Ferritin-H mRNA 5'UTR is shown in Figure 11. The human Ferritin-H mRNA 5'UTR shows a high degree of secondary structure, with numerous stem-loops, which is expected due to the high GC content in the RNA sequence. Interestingly, the

predicted structure does not contain a single stem-loop IRE where expected at nucleotide positions 61-88, as suggested by the presence of an apical loop that contains a CAGUGC sequence. In order to form the IRE stem-loop, nucleotides 68-72 should pair with nucleotides 83-79. However, in Figure 11, nucleotides 68-72 show medium to high SHAPE reactivities and are single-stranded, whereas nucleotides 79-82 pair with nucleotides 125, 123, 122, and 121, respectively. Based on the structure prediction, nucleotides at the 5'-end of the human Ferritin-H mRNA 5'UTR (nucleotides 2-10) form base pairs with nucleotides at the 3'-end of the RNA; this base-pairing may disrupt the secondary structure of the other regions in this RNA. We thus deleted 30 nucleotides from the 3'-end of the RNA, and synthesized an RNA named "human Ferritin-H mRNA short 5'UTR".
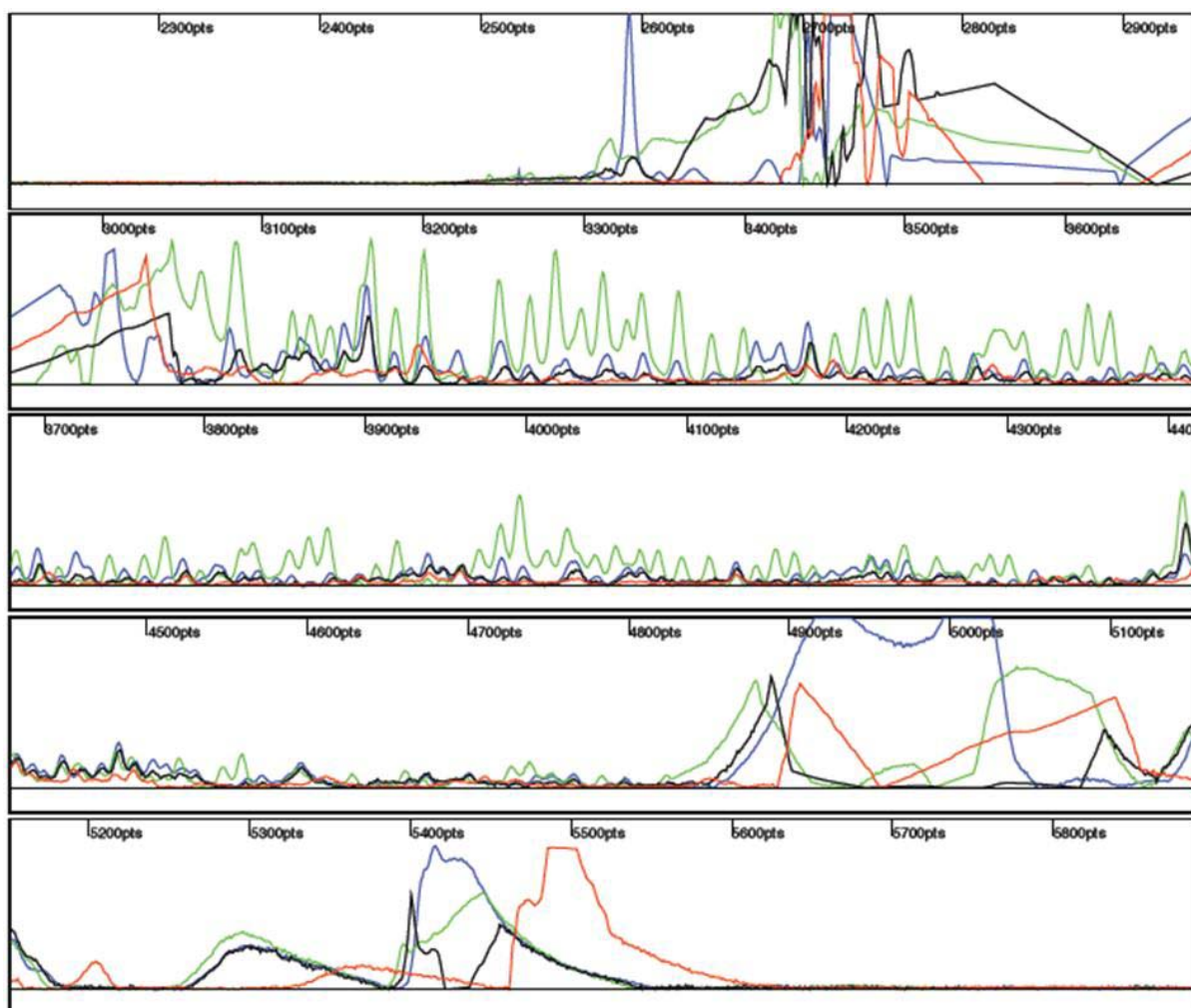
Figure 9. SHAPE data for the 5'UTR of the human Ferritin-H mRNA transcript. The raw output from the ABI 310 genetic analyzer underwent baseline adjustment, matrixing, and mobility shift adjustment. Fluorescence-labeled DNA primer was annealed to the 3'-end of this 237-nucleotide RNA. The blue trace is the +1M7 sample; the black trace is the -1M7 negative control; green and red traces are two dideoxy ladders (ddG and ddT, respectively). The x-axis indicates the number of data points collected. The y-axis (not shown) enumerates the fluorescence units.
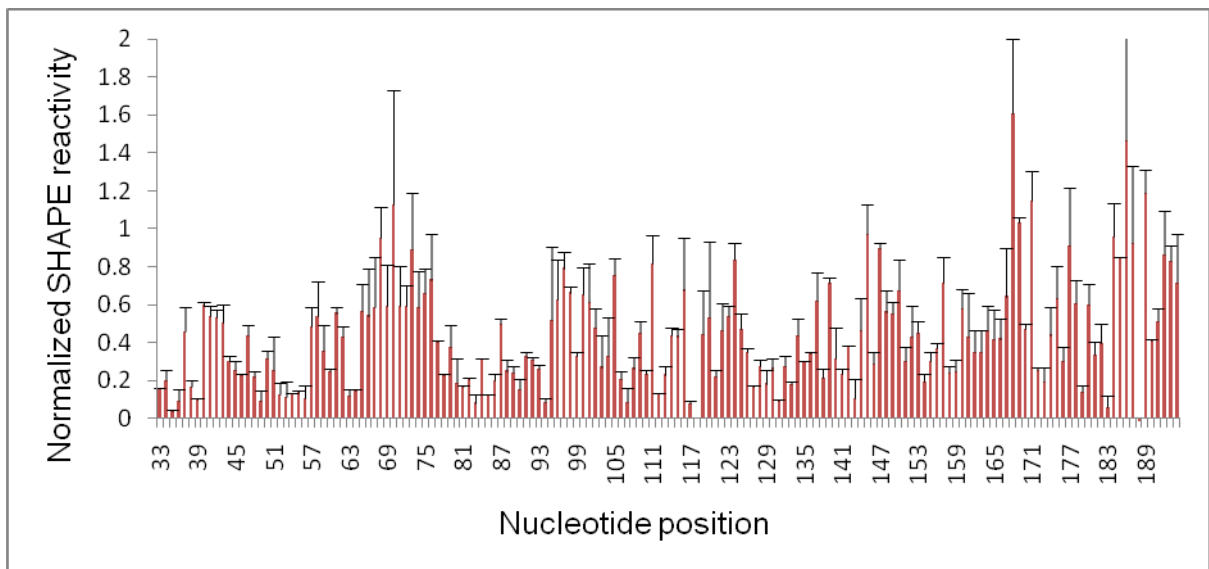
Figure 10. Single nucleotide resolution of normalized SHAPE reactivities for the human Ferritin-H mRNA 5'UTR. Error bars represent standard deviations calculated from two independent experiments.
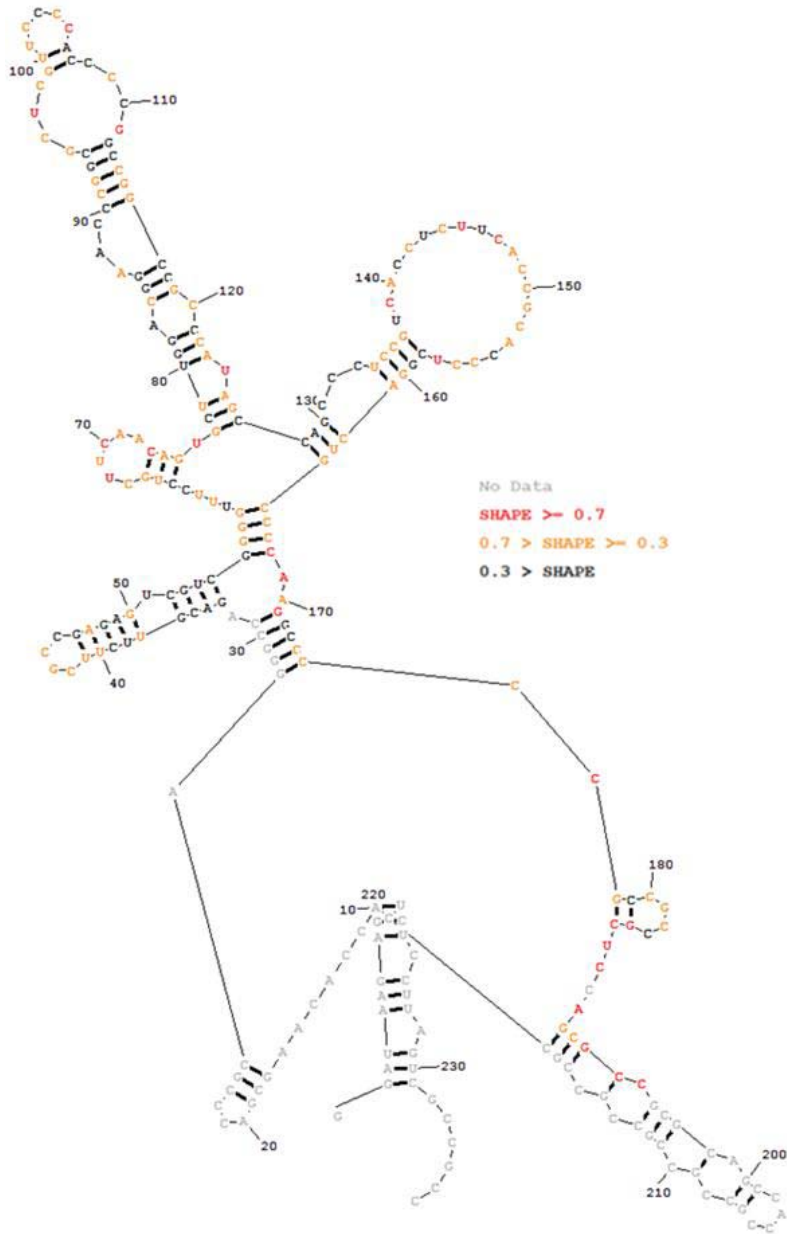
Figure 11. The pred icted secondary structure of t he 5'U TR of hu man Ferritin-H mRNA. Nucleotides a re c olored bl ack (unreactive, S HAPE r eactivity < 0.3), or ange (moderately reactive, $0.3 \leq$ SHAPE reactivity <0.7), red (highly reactive, SHAPE reactivity ≥ 0.7), or grey (no data).

3.2. Human Ferritin-H mRNA short 5'UTR

The sequence of the 207-nucleotide-long human Ferritin-H mRNA short 5'UTR is as follows:

5'-GG AUAAGAGACC ACAAGCGACC CGCAGGGCCA GACGUUCUUC GCCGAGAGUC GUCGGGGUUU CCUGCUUCAA CAGUGCUUGG ACGGAACCCG GCGCUCGUUC CCCACCCCGG CCGGCCGCCC AUAGCCAGCC CUCCGUCACC UCUUCACCGC ACCCUCGGAC UGCCCCAAGG CCCCCGCCGC CGCUCCAGCG CCGCGCAGCC ACCGC-3'

3.2.1. AFM images

An AFM image of the human Ferritin-H mRNA short 5'UTR is shown in Figure 12. The 207-nucleotide-long RNA molecule folds into a complex three-dimensional structure that appears as a blob on the mica surface. The heights of eight blobs were measured as: 1.12 nm, 0.85 nm, 0.79 nm, 0.60 nm, 0.59 nm, 0.50 nm, 0.34 nm, and 0.41 nm (average $\pm$ standard deviation = 0.65 ± 0.26 nm). The volumes of the same eight blobs were 2403 nm^3, 2001 nm^3, 1451 nm^3, 941 nm^3, 694 nm^3, 982 nm^3, 471 nm^3, and 357 nm^3, respectively (average $\pm$ standard deviation = 1162 ± 732 nm^3). The averaged volume of the blobs for the human Ferritin-H mRNA short 5'UTR (1162 ± 732 nm^3) doubles that of the human Ferritin-H 5'UTR (356 ± 360 nm^3), which demonstrates that no correlation has been observed between volume and RNA sequence length in this study.

A
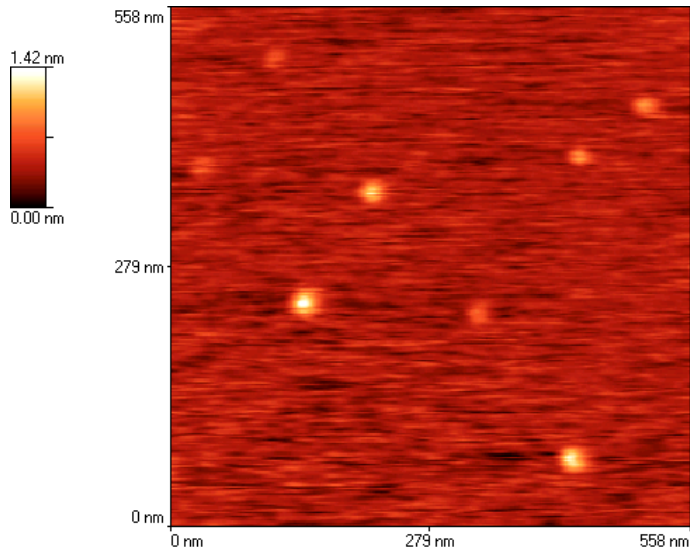
B
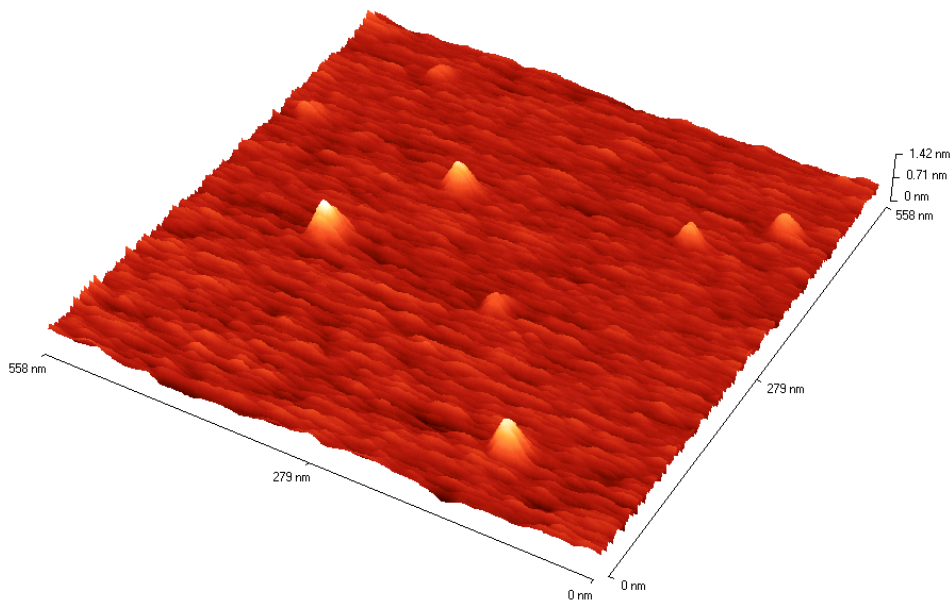
Figure 12. AFM images of a sample composed of the human Ferritin-H mRNA short

5'UTR deposited onto a mica surface. (A) The two-dimensional view of the sample surface,

and (B) the three-dimensional view of the sample surface.

3.2.2. SHAPE data

The human Ferritin-H mRNA short 5'UTR transcripts were folded in a solution containing 6 mM Mg^{2+} and subjected to the SHAPE procedure. The SHAPE experiments were repeated at least twice. Figure 13 illustrates one set of SHAPE electropherograms of this RNA. Figure 14 presents the averaged SHAPE reactivities from two SHAPE experiments. The predicted structure with the lowest free energy for the human Ferritin-H mRNA short 5'UTR is shown in Figure 15.

Human Ferritin-H mRNA short 5'UTR forms the correct IRE stem-loop structure at nucleotide positions 61-88, including a 73CAGUGC78 apical loop. It is known that C73 pairs with G77 within the loop, which is required for efficient IRP protein binding.[12] Figure 16 shows that G77 is unreactive (i.e., low SHAPE reactivity) due to its involvement in the base pairing. The 65UGC67 and C84 nucleotides form a bulge in the RNA, which is a conserved feature for the ferritin mRNAs. The G66-C84 base pair is also required for IRP binding. The crystal structure of the IRP1-ferritin IRE complex resolved by Volz's research group has shown that the L-shaped IRP1 interacts with the ferritin IRE stem-loop at two positions, the apical loop and the bulge.[85,86]

SHAPE data from the human ferritin-H mRNA short 5'UTR demonstrate that the left side of the stem (68UUCAA72) of the IRE is more reactive than the right side of the stem (83AGGUU79), which means that the left side may be adopting a conformation that brings it toward the outside of the RNA, where it would be more accessible to 1M7.

Figure 13. SHAPE d ata f or the 5' UTR of the hum an Ferritin-H m RNA s hort transcript. The r aw output f rom t he A BI 310 ge netic a nalyzer unde rwent ba seline adjustment, matrixing, and mobility shift adjustment. Fluorescence-labeled DNA primer was annealed to the 3'-end of this 207-nucleotide RNA. The blue trace is the +1M7 sample; the black trace is the -1M7 negative control; green and red traces are two dideoxy ladders (ddG and ddA, respectively). The x-axis indicates the number of data points collected. The y-axis (not shown) enumerates the fluorescence units.

38

Figure 14. Single nucleotide resolution of normalized SHAPE reactivities for the human Ferritin-H mRNA short 5'UTR. Error bars represent standard deviations calculated from two independent experiments.

Figure 15. The predicted secondary structure of the 5' UTR of the human Ferritin-H mRNA short transcript. Nucleotides are colored black (unreactive, SHAPE reactivity <0.3), orange (moderately reactive, $0.3 \leq$ SHAPE reactivity <0.7), red (highly reactive, SHAPE reactivity ≥ 0.7), or grey (no data).

3.3. Mouse Ferritin-H mRNA 5'UTR

The sequence of the 169-nucleotide-long mouse Ferritin-H mRNA 5'UTR is as follows:

5'-GG CAGACGUUCU CGCCCAGAGU CGCCGCGGUU UCCUGCUUCA ACAGUGCUUG AACGGAACCC GGUGCUCGAC CCCUCCGACC CCCGCCGGCC GCUUCGAGCC UGAGCCCUUU GCAACUUCGU CGUUCCGCCG CUCCAGCGUC GCCACCGCGC CUCGCCCCGC CGCCACC-3'

3.3.1. AFM images

An AFM image of the mouse Ferritin-H mRNA 5'UTR is shown in Figure 16. The 169-nucleotide-long RNA molecule folds into a complex three-dimensional structure that appears as a blob on the mica surface. The heights of five blobs were measured as: 0.73 nm, 0.59 nm, 0.53 nm, 0.48 nm, and 0.30 nm (average ± standard deviation = 0.53 ± 0.16 nm). The volumes of the same five blobs were 1136 nm^3, 851 nm^3, 555 nm^3, 468 nm^3, and 680 nm^3, respectively (average ± standard deviation = 738 ± 265 nm^3).

A
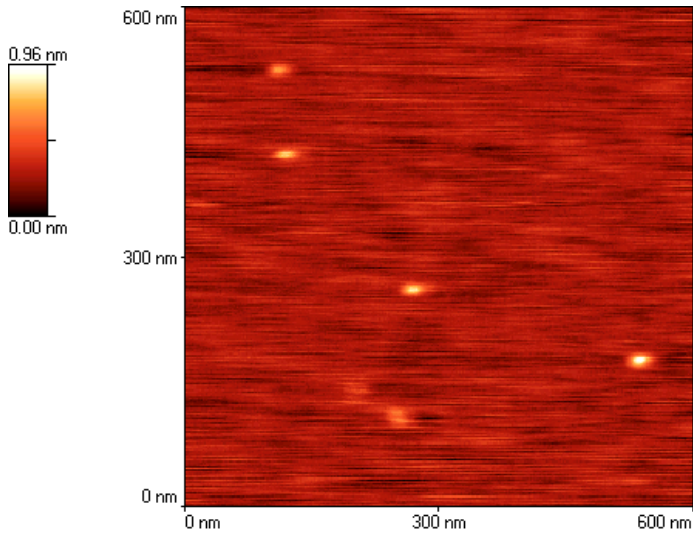
B

Figure 16. AFM i mages of a sa mple com posed of t he m ouse F erritin-H m RNA 5'UTR deposited onto a mica surface. (A) The two-dimensional view of the sample surface, and (B) the three-dimensional view of the sample surface.

3.3.2. SHAPE data

The mouse Ferritin-H mRNA 5'UTR transcripts were folded in a solution containing 6 mM Mg^{2+} and subjected to the SHAPE procedure. The SHAPE experiments were repeated at least twice. Figure 17 illustrates one set of SHAPE electropherograms of this RNA. Figure 18 presents the averaged SHAPE reactivities from two SHAPE experiments. The predicted structure with the lowest free energy for the mouse Ferritin-H mRNA 5'UTR is shown in Figure 19.

Mouse Ferritin-H mRNA 5'UTR forms the correct IRE stem-loop structure at nucleotide positions 29-61, including a 44CAGUGC49 apical loop. The 36UGC38 and C55 nucleotides form a bulge in the RNA. SHAPE data from the mouse ferritin-H mRNA 5'UTR demonstrate that nucleotides in the apical loop and the bulge of the RNA are reactive; nucleotides in the stem of the IRE are unreactive.
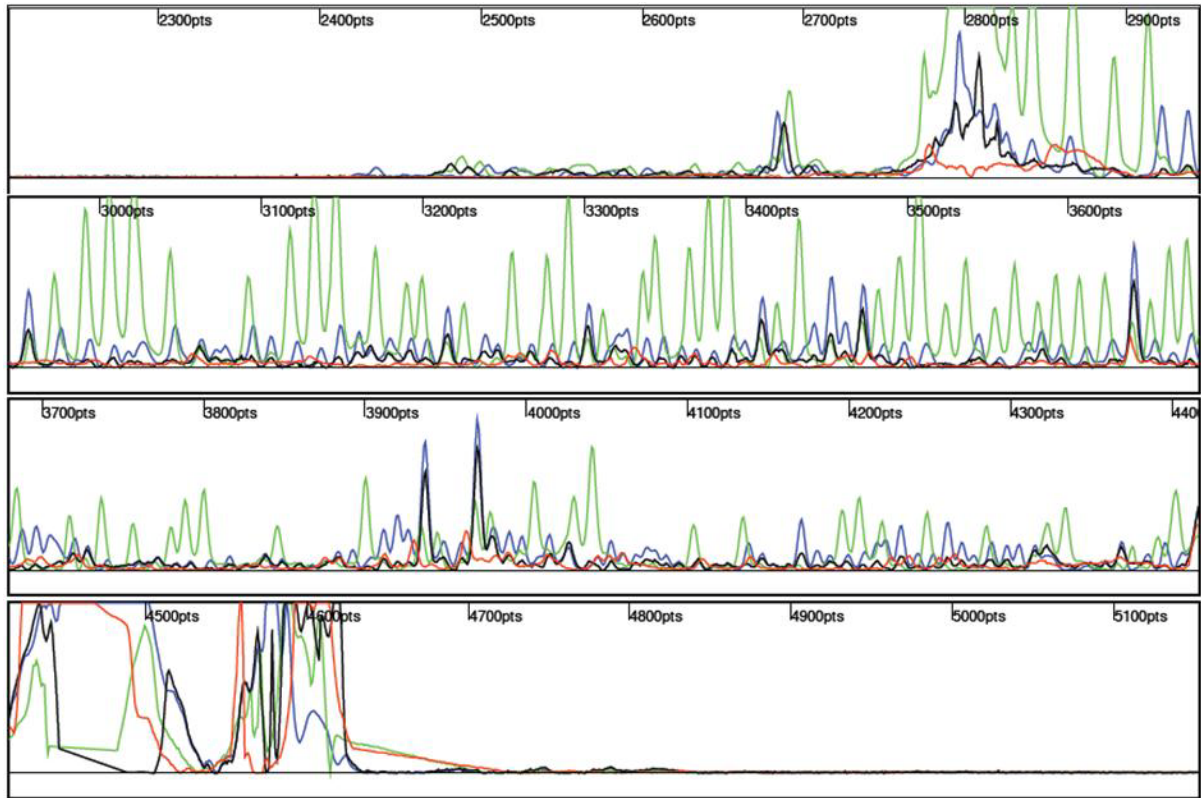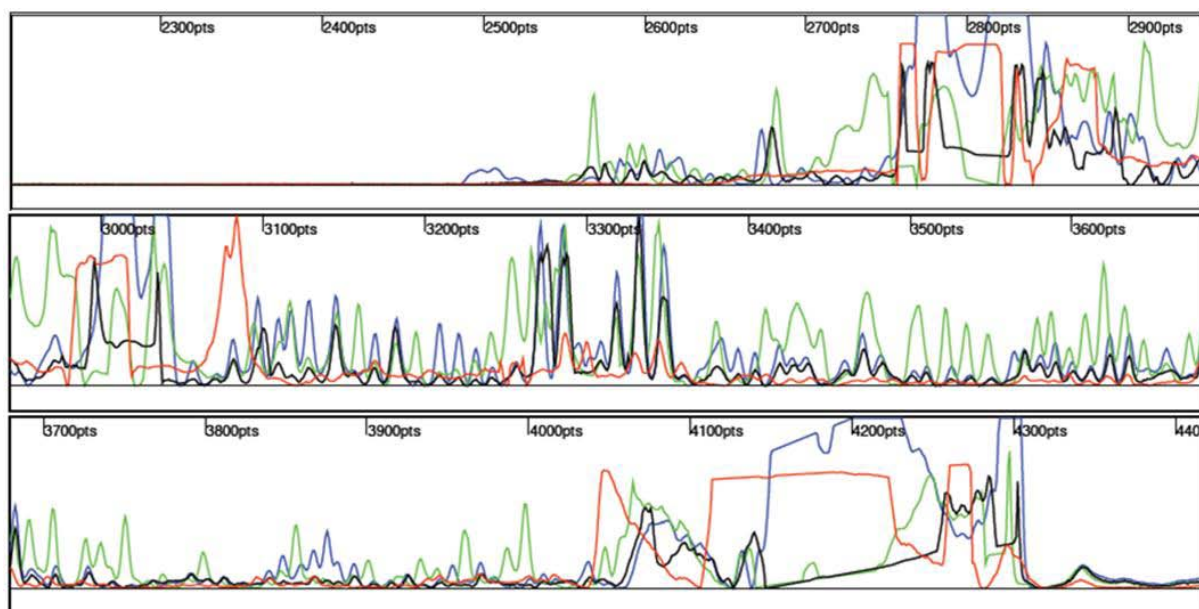
Figure 17. SHAPE data for the 5'UTR of the mouse Ferritin-H mRNA transcript. The raw output from the ABI 310 genetic analyzer underwent baseline adjustment, matrixing, and mobility shift adjustment. Fluorescence-labeled DNA primer was annealed to the 3'-end of this 169-nucleotide RNA. The blue trace is the +1M7 sample; the black trace is the -1M7 negative control; green and red traces are two dideoxy ladders (ddG and ddA, respectively). The x-axis indicates the number of data points collected. The y-axis (not shown) enumerates the fluorescence units.
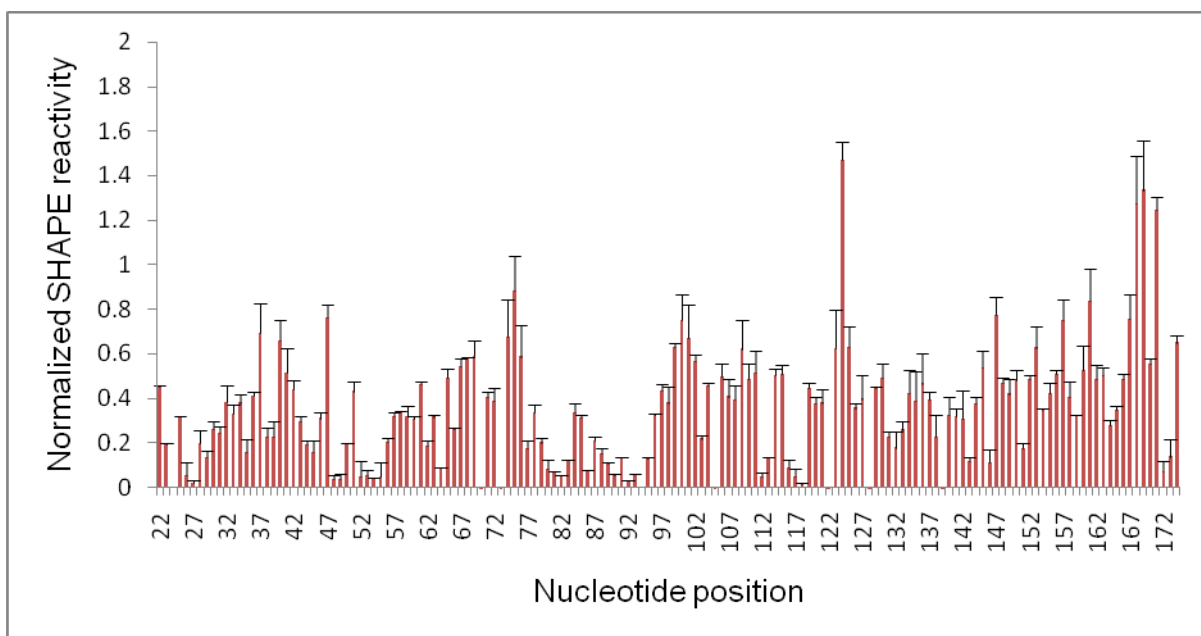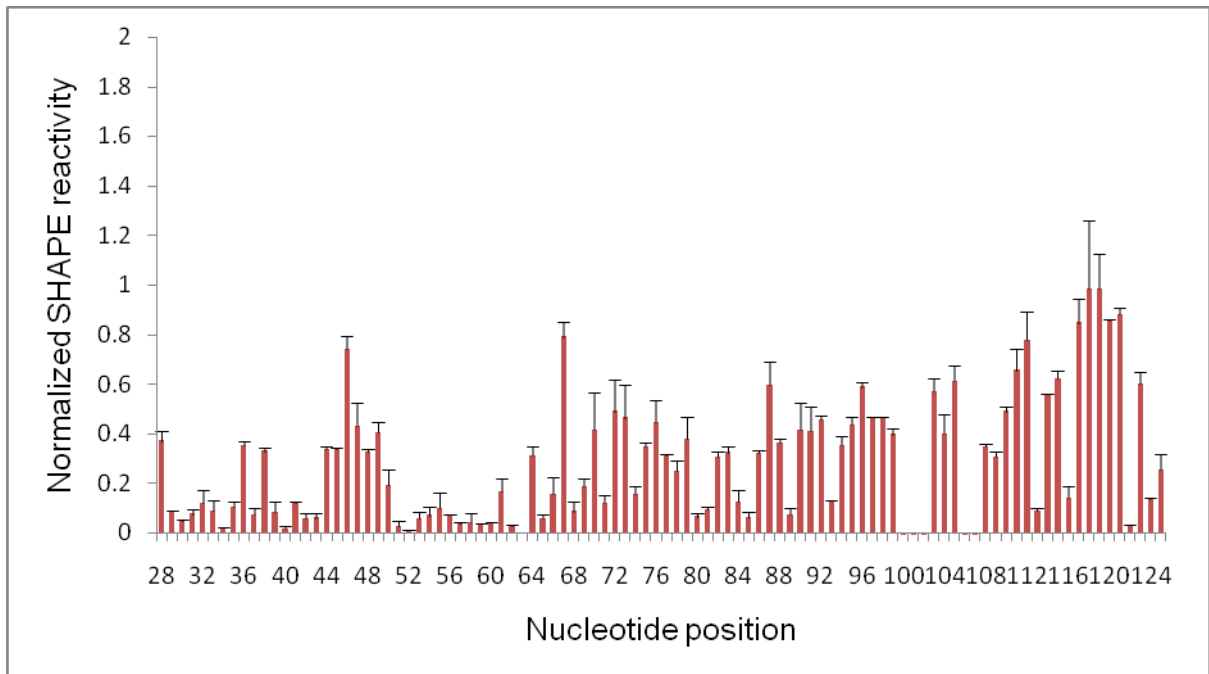
Figure 18. Single nucleotide resolution of normalized SHAPE reactivities for the mouse Ferritin-H mRNA 5'UTR. Error bars represent standard deviations calculated from two independent experiments.
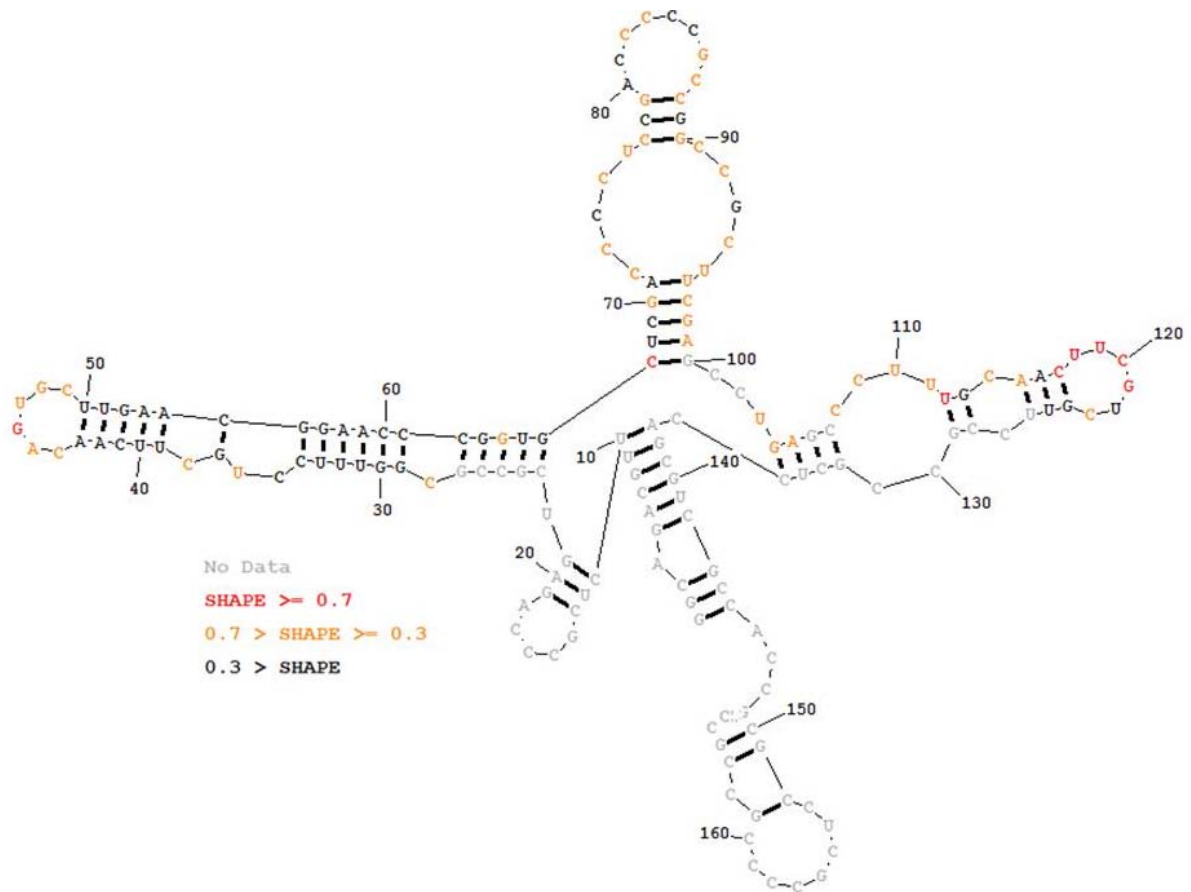
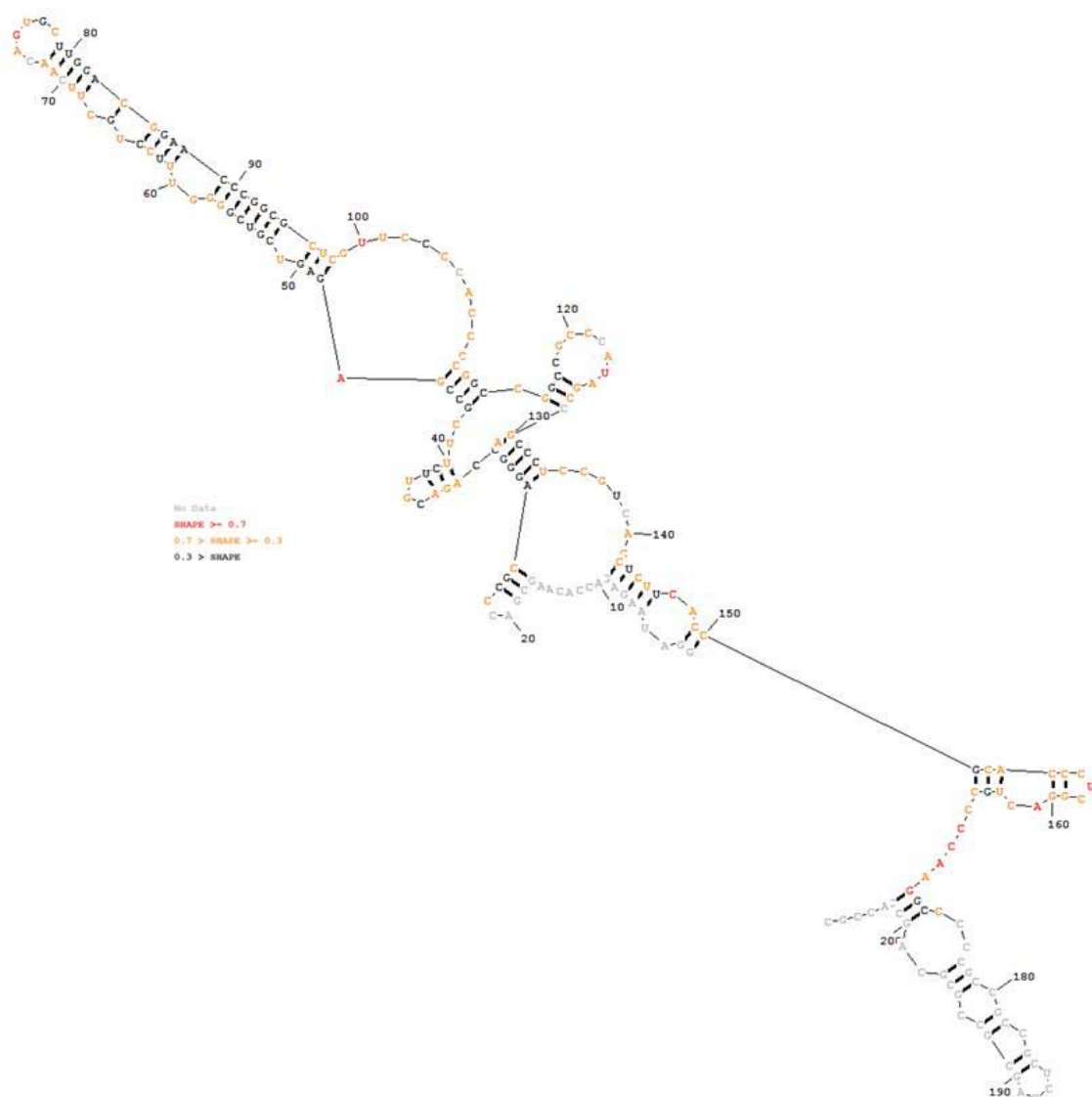**Figure 19.** The predicted secondary structure of the 5' UTR of the mouse Ferritin-H mRNA t ranscript. Nucleotides are colo red black (unreactive, S HAPE r eactivity <0.3), orange (moderately r eactive, $0.3 \leq$ SHAPE reactivity <0.7), red (highly reactive, SHAPE reactivity ≥ 0.7), or grey (no data).

3.4. Human Ferritin-L mRNA 5'UTR

The sequence of the 217-nucleotide-long RNA, which contains the 201-nucleotide-long human Ferritin-L mRNA 5'UTR plus 16 nucleotides that extend into the coding region of the human Ferritin-L mRNA, is shown below.

5'-GG GCAGUUCGGC GGUCCCGCGG GUCUGUCUCU UGCUUCAACA GUGUUUGGAC GGAACAGAUC CGGGGACUCU CUUCCAGCCU CCGACCGCCC UCCGAUUUCC UCUCCGCUUG CAACCUCCGG GACCAUCUUC UCGGCCAUCU CCUGCUUCUG GGACCUGCCA GCACCGUUUU UGUGGUUAGC UCCUUCUUGC CAACCAACCA UGAGCUCCCA GAUUC-3'

3.4.1. AFM images

An AFM image of the human Ferritin-L mRNA 5'UTR is shown in Figure 20. The RNA molecule folds into a complex three-dimensional structure that appears as a blob on the mica surface. The heights of fourteen blobs were measured as: 1.22 nm, 1.35 nm, 1.33 nm, 0.55 nm, 1.23 nm, 0.81 nm, 0.77 nm, 0.93 nm, 0.88 nm, 0.83 nm, 0.94 nm, 1.35 nm, 1.19 nm, and 0.81 nm (average ± standard deviation = 1.01 ± 0.26 nm). The volumes of the same fourteen blobs were 3355 nm^3, 4407 nm^3, 5845 nm^3, 943 nm^3, 2711 nm^3, 768 nm^3, 1241 nm^3, 1671 nm^3, 1404 nm^3, 1463 nm^3, 2780 nm^3, 1384 nm^3, 3212 nm^3, and 1241 nm^3, respectively (average ± standard deviation = 2316 ± 1481 nm^3).
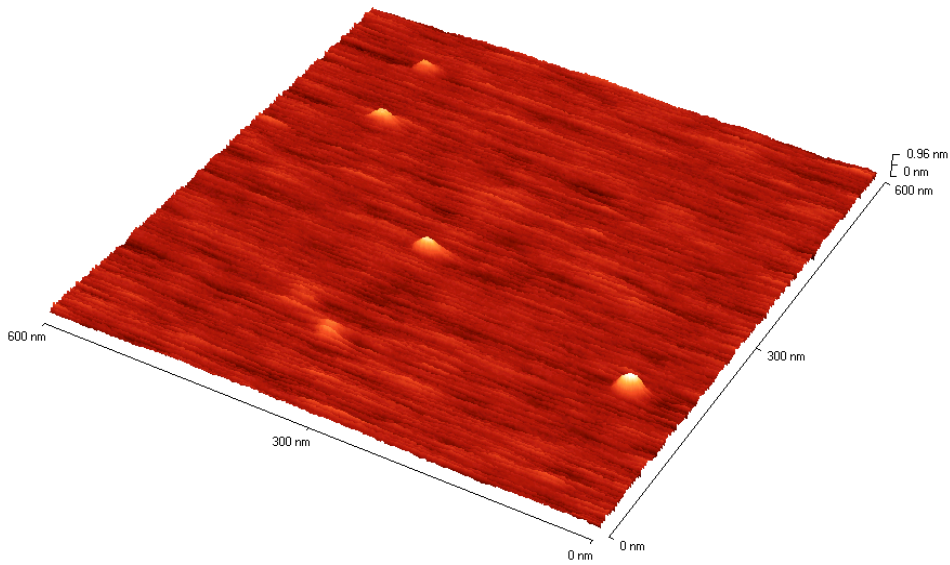
A
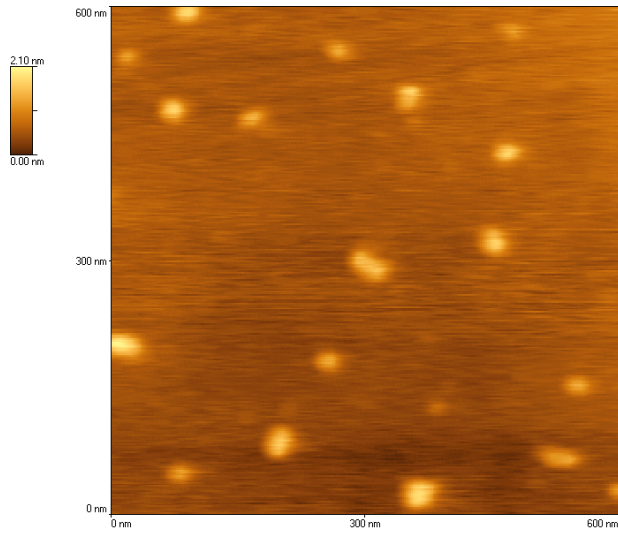
B

Figure 20. AFM i mages of a sa mple com posed of t he hu man Ferritin-L m RNA 5'UTR deposited onto a mica surface. (A) The two-dimensional view of the sample surface, and (B) the three-dimensional view of the sample surface.

48

3.4.2. SHAPE data

The human Ferritin-L mRNA 5'UTR transcripts were folded in a solution containing 6 mM Mg^{2+} and subjected to the SHAPE procedure. The SHAPE experiments were repeated at least twice. The predicted structure with the lowest free energy for the human Ferritin-L mRNA 5'UTR is shown in Figure 21. Human Ferritin-L mRNA 5'UTR forms the correct IRE stem-loop structure at nucleotide positions 27-57, including a 41CAGUGU46 apical loop. The 33UGC35 and C52 nucleotides form a bulge in the RNA.

Figure 21. The predicted secondary structure of the 5'UTR of the human Ferritin-L mRNA tra nscript. Nucleotides ar e colored black (unreactive, S HAPE r eactivity < 0.3), orange (moderately r eactive, 0.3 ≤ SHAPE reactivity <0.7), red (highly reactive, SHAPE reactivity ≥0.7), or grey (no data).

3.5. Mouse Ferritin-L mRNA 5'UTR

The sequence of the 207-nucleotide-long mouse Ferritin-L mRNA 5'UTR is as follows:

5'-GA GCAGCGCCUU GGAGGUCCCG UGGAUCUGUG UCUUGCUUCA ACAGUGUUUG AACGGAACAG ACCCGGGGAU UCCCACUGUA CUCGCUUCCA GCCGCCUUUA CAAGUCUCUC CAGUCGCAGC CUCCGGGACC AUCUCCUCGC UGCCUUCAGC UCCUAGGACC AGUCUGCACC GUCUCUUCGC GGUUAGCUCC UACUCCGGAU CAGCC-3'

3.5.1. AFM images

An AFM image of the mouse Ferritin-L mRNA 5'UTR is shown in Figure 22. The RNA molecule folds into a complex three-dimensional structure that appears as a blob on the mica surface. The heights of fourteen blobs were measured as: 0.78 nm, 0.92 nm, 1.04 nm, 0.64 nm, 0.83 nm, 0.65 nm, 0.90 nm, 0.87 nm, 1.02 nm, 0.96 nm, 0.61 nm, 0.81 nm, 0.90 nm, and 0.70 nm (average ± standard deviation = 0.83 ± 0.14 nm). The volumes of the same fourteen blobs were 1103 nm^3, 1183 nm^3, 1022 nm^3, 782 nm^3, 828 nm^3, 709 nm^3, 952 nm^3, 1040 nm^3, 933 nm^3, 1220 nm^3, 486 nm^3, 749 nm^3, 1365 nm^3, and 619 nm^3, respectively (average ± standard deviation = 928 ± 247 nm^3).
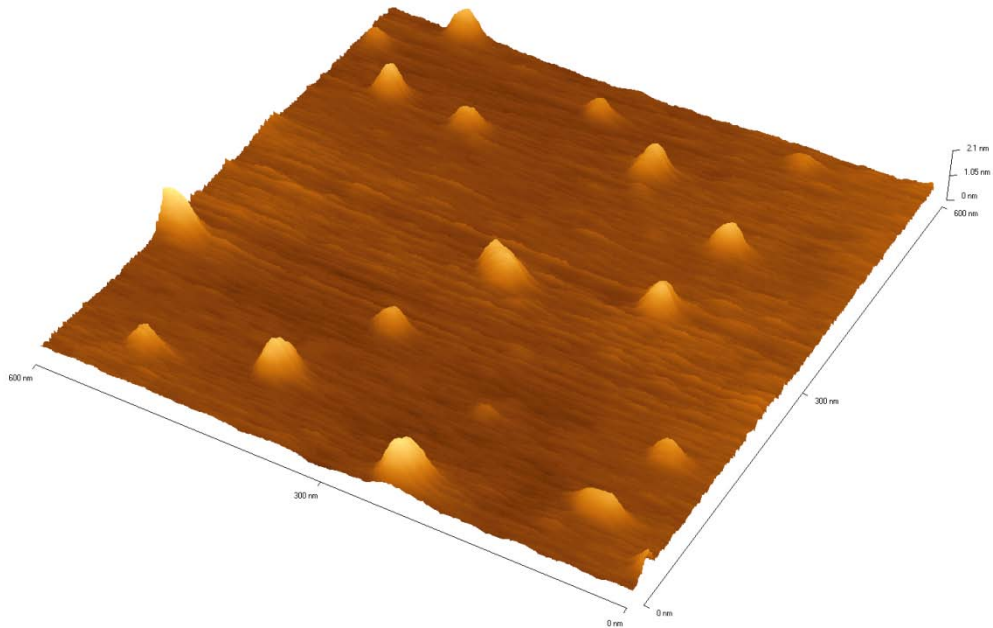
A
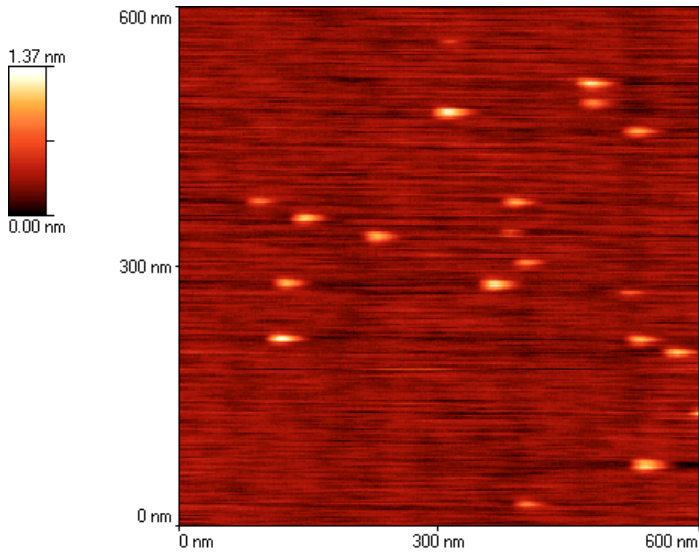
B

Figure 22. AFM i mages of a sam ple com posed of t he mouse Ferritin-L mR NA 5'UTR deposited onto a mica surface. (A) The two-dimensional view of the sample surface, and (B) the three-dimensional view of the sample surface.

51

3.5.2. SHAPE data

The mouse Ferritin-L mRNA 5'UTR transcripts were folded in a solution containing

6 mM Mg^{2+} and subjected to the SHAPE procedure. The SHAPE experiments were repeated

at least twice. The predicted structure with the lowest free energy for the mouse Ferritin-L

mRNA 5'UTR is shown in Figure 23. Mouse Ferritin-L mRNA 5'UTR forms the correct

IRE stem-loop structure at nucleotide positions 30-60, including a 44CAGUGU49 apical

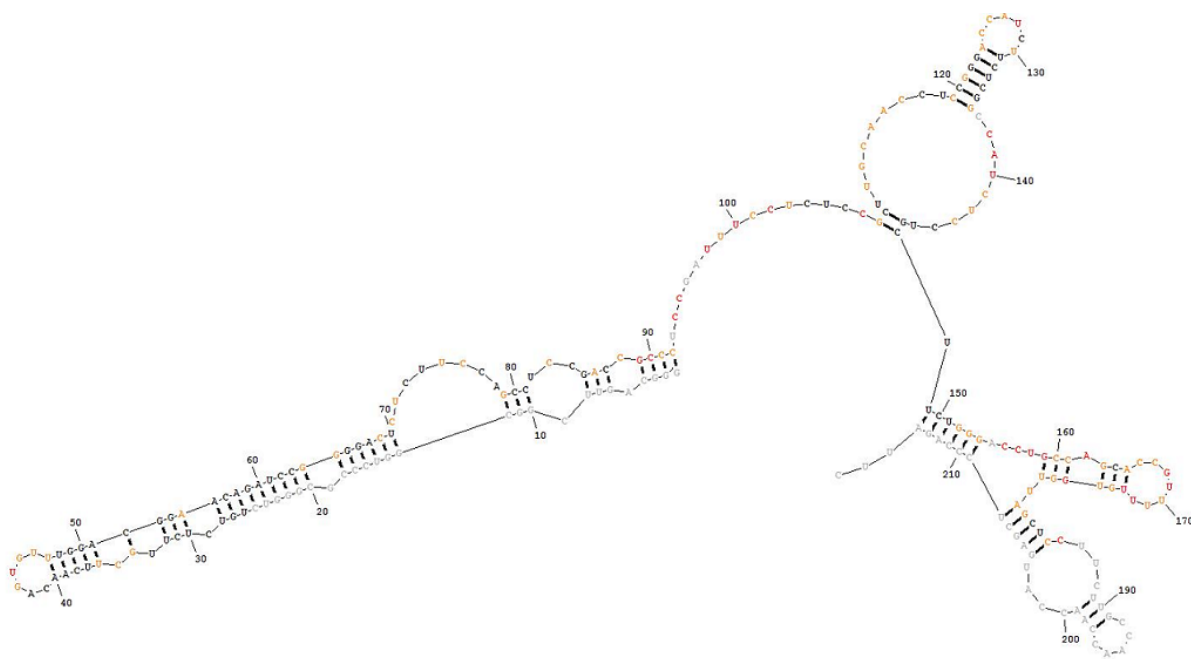loop. The 36UGC38 and C55 nucleotides form a bulge in the RNA.

Figure 23. The predicted secondary structure of the 5'UTR of the mouse Ferritin-L

mRNA tra nscript. Nucleotides are colo red black (unreactive, S HAPE r eactivity <0.3),

orange (moderately r eactive, $0.3 \leq$ SHAPE reactivity <0.7), red (highly reactive, SHAPE

reactivity ≥ 0.7), or grey (no data).

3.6. Human APP mRNA 5'UTR

The sequence of the 163-nucleotide-long RNA, which contains the 149-nucleotide-long human APP mRNA 5'UTR plus 14 nucleotides that extend into the coding region of the human APP mRNA, is shown below.

5'-GG AGUUUCCUCG GCAGCGGUAG GCGAGAGCAC GCGGAGGAGC

GUGCGCGGGG GCCCCGGGAG ACGGCGGCGG UGGCGGCGCG GGCAGAGCAA

GGACGCGGCG GAUCCCACUC GCACAGCAGC GCACUCGGUG CCCCGCGCAG

GGUCGCG AUGCUGCCCG GUUU-3'

3.6.1. AFM images

An AFM image of the human APP mRNA 5'UTR is shown in Figure 24. The RNA molecule folds into a complex three-dimensional structure which appears as a blob on the mica surface. The heights of three blobs were measured as: 0.37 nm, 0.40 nm, and 0.35 nm (average ± standard deviation = 0.37 ± 0.03 nm). The volumes of the same three blobs were 476 nm^3, 546 nm^3, and 408 nm^3, respectively (average ± standard deviation = 477 ± 69 nm^3).

A
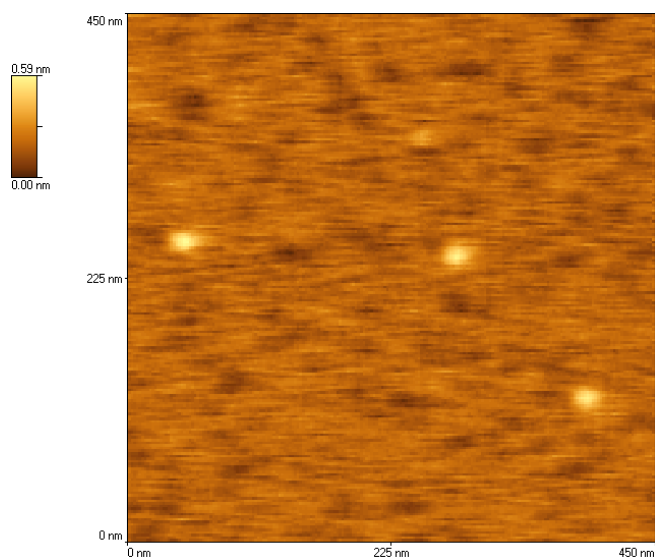
B

Figure 24. AFM images of a sample composed of the human APP mRNA 5' UTR deposited onto a mica surface. (A) The two-dimensional view of the sample surface, and (B) the three-dimensional view of the sample surface.

3.6.2. SHAPE data
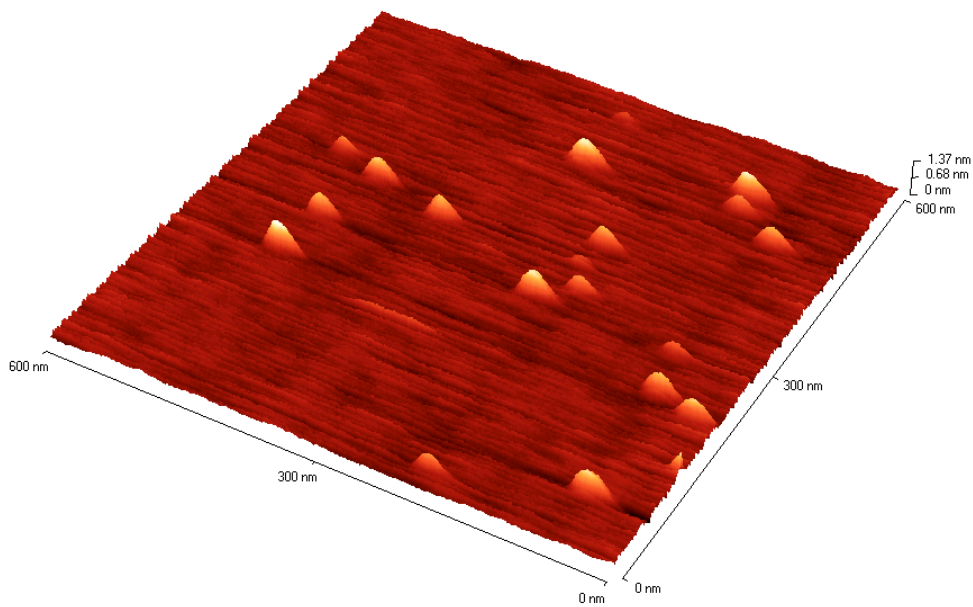
The human APP mRNA 5'UTR transcripts were folded in a solution containing 6 mM Mg^{2+} and subjected to the SHAPE procedure. The SHAPE experiments were repeated at least twice. Figure 25 illustrates one set of SHAPE electropherograms of this RNA. Figure 26 presents the averaged SHAPE reactivities from two SHAPE experiments. The predicted structure with the lowest free energy for the human APP mRNA 5'UTR is shown in Figure 27.

The human APP mRNA 5'UTR contains an IRE stem-loop structure that is different from the IREs in the 5'UTRs of the Ferritin-H and Ferritin-L mRNAs; therefore, it is named IRE-Type II. Instead of having a 6-nucleotide apical loop comprised of CAGUGN (N can be A, C, or U, but not G), as present in the Ferritin IREs, the human APP IRE contains a 13-nucleotide loop comprised of nucleotides 83GGCAGAGCAAGGA95 (see Figure 27). The 85CAGA88 sequence in the apical loop is called an "amyloid" CAGA box. The mammal CAGA box is a Smad protein binding site for Smad3 and Smad4.[87] The "amyloid" CAGA box within the IRE region of the human APP mRNA 5'UTR is believed to provide additional regulation of the synthesis of the human APP protein and to facilitate the production of Aβ.[87]

In addition to the difference in the apical loop, nucleotides 79CGCG82 in the human APP mRNA 5'UTR pair with nucleotides 99GCGC96 to form a 4-base-pair stem, whereas

IREs in the ferritin mRNA 5'UTRs have a conserved 5-base-pair stem. In addition, instead of having a UGC-C type of bulge, the human APP IRE contains a 78G-G100 bulge.

In the human APP mRNA 5'UTR, most nucleotides within positions 101-123 are reactive, which means that these nucleotides may adopt a conformation that makes them more accessible to 1M7. Interestingly, this RNA region is located within the interleukin-1 responsive element (called the acute box) domain, where interleukin-1, a cytokine released early in the acute phase of the immune response, binds in order to regulate and stimulate APP protein synthesis.

Figure 25. SHAPE data for the 5'UTR of the human APP mRNA transcript. The raw output from the ABI 310 genetic analyzer underwent baseline adjustment, matrixing, and mobility shift adjustment. Fluorescence-labeled DNA primer was annealed to the 3'-end of this 163-nucleotide RNA. The blue trace is the +1M7 sample; the black trace is the -1M7 negative control; green and red traces are two dideoxy ladders (ddG and ddT, respectively).

The x-axis indicates the number of data points collected. The y-axis (not shown) enumerates the fluorescence units.

Figure 26. Single nuc leotide r esolution of nor malized SHAPE re activities f or the human APP m RNA 5' UTR.   Error ba rs re present s tandard de viations calculated f rom tw o independent experiments.
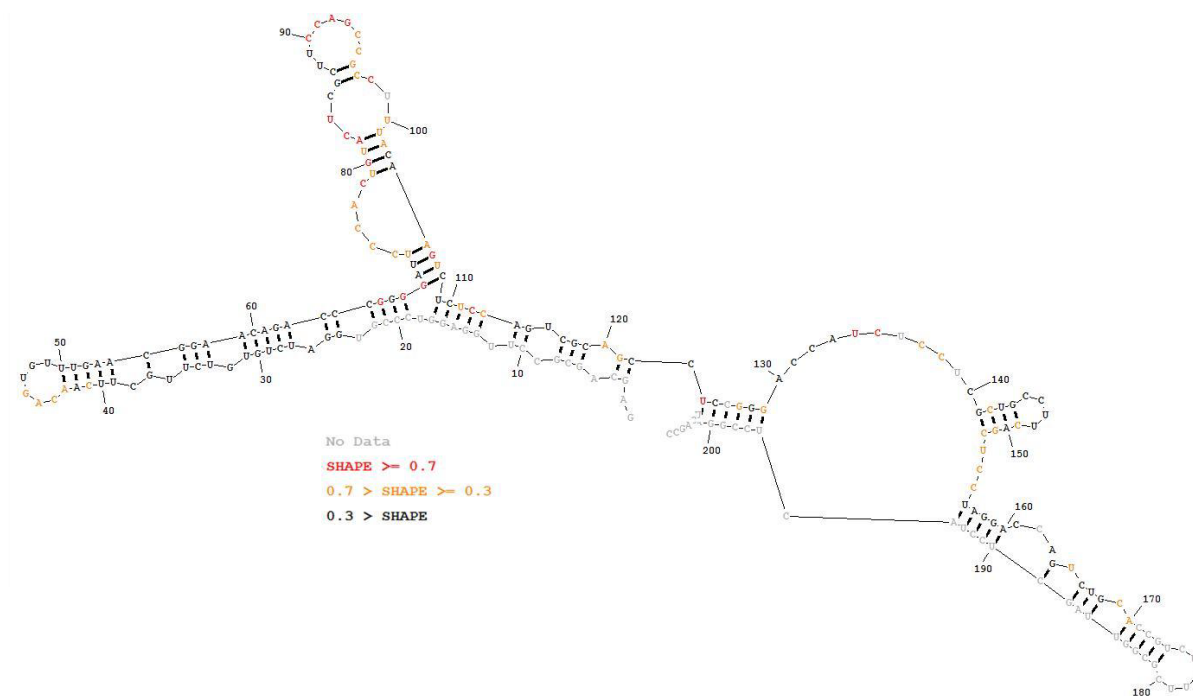
Figure 27. The pred icted secondary structure of t he 5'U TR of t he human APP mRNA t ranscript. Nucleotides are colo red black (unreactive, S HAPE r eactivity <0.3), orange (moderately r eactive, 0.3 ≤ SHAPE reactivity <0.7), red (highly reactive, SHAPE reactivity ≥0.7), or grey (no data).

3.7. Mouse APP mRNA 5'UTR

The sequence of the 147-nucleotide-long mouse APP mRNA 5'UTR is as follows:
5'-GG GUUUCCUCGG CGGCGGGAGG CGAGAGCACC GGGAGCAGAG

CGAGCGCGGG GCCACCGGAG ACGGCGGCGG CGGCGCGGAC ACAGCCAGGG

CGCGGCGGAU CUUCCACUCG CACACGGAGC ACUCGGUGGC CCACGCAGGA

UCACG-3'

3.7.1. AFM images

An AFM image of the mouse APP mRNA 5'UTR is shown in Figure 28. The RNA
molecule folds into a complex three-dimensional structure that appears as a blob on the mica
surface. The heights of five blobs were measured as: 2.60 nm, 2.90 nm, 2.50 nm, 2.90 nm,
and 1.90 nm (average $\pm$ standard deviation = 2.56 $\pm$ 0.41 nm). The volumes of the same five
blobs were 2509 nm^3, 1881 nm^3, 1054 nm^3, 2006 nm^3, and 1162 nm^3, respectively (average $\pm$
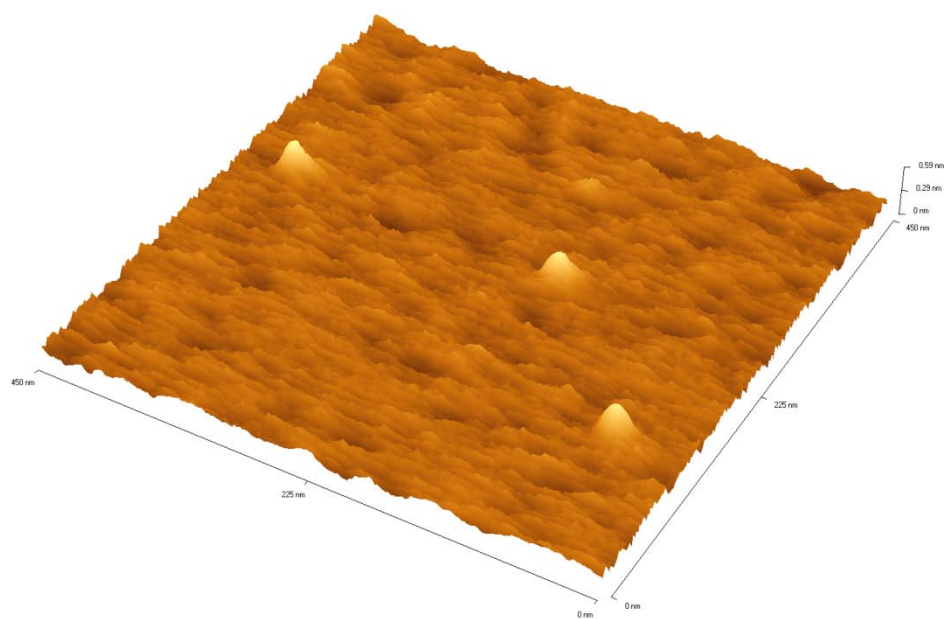standard deviation = 1722 $\pm$ 609 nm^3).

A
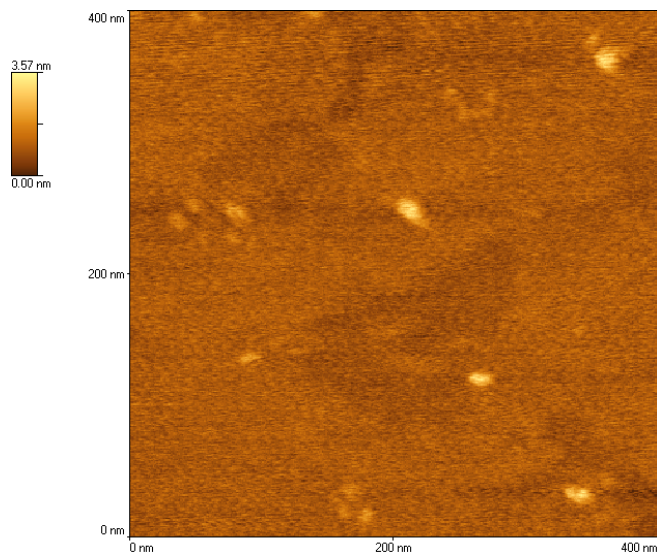
B
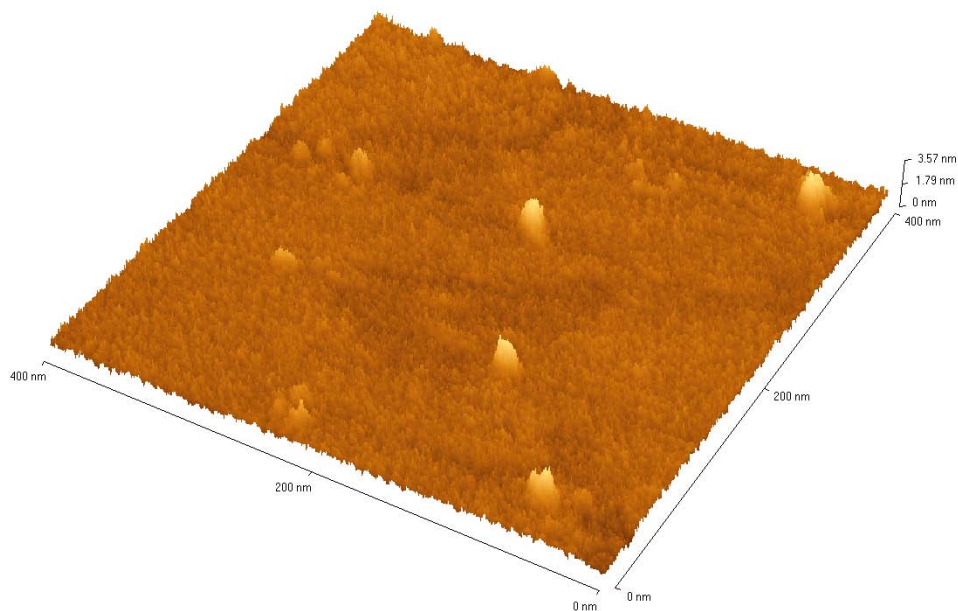
Figure 28. AFM images of a sample composed of the mouse APP mRNA 5'UTR deposited onto a mica surface. (A) The two-dimensional view of the sample surface, and (B) the three-dimensional view of the sample surface.

3.7.2. SHAPE data

The mouse APP mRNA 5'UTR transcripts were folded in a solution containing 6 mM Mg^{2+} and subjected to the SHAPE procedure. The SHAPE experiments were repeated at least twice. Figure 29 illustrates one set of SHAPE electropherograms of this RNA. Figure 30 presents the averaged SHAPE reactivities from two SHAPE experiments. The predicted structure with the lowest free energy for the mouse APP mRNA 5'UTR is shown in Figure 31.

The IRE-like stem-loop structure in the mouse APP mRNA 5'UTR contains a 9-nucleotide apical loop comprised of nucleotides 77GCGGACACA85, which does not contain an "amyloid" CAGA sequence. Nucleotides 74GGC76 pair with nucleotides 88CCG86 to form a 3-base-pair stem (see Figure 31). Rather than having the UGC-C type of bulge present in the ferritin IREs, the predicted mouse APP IRE structure contains a 6-nucleotide internal loop.
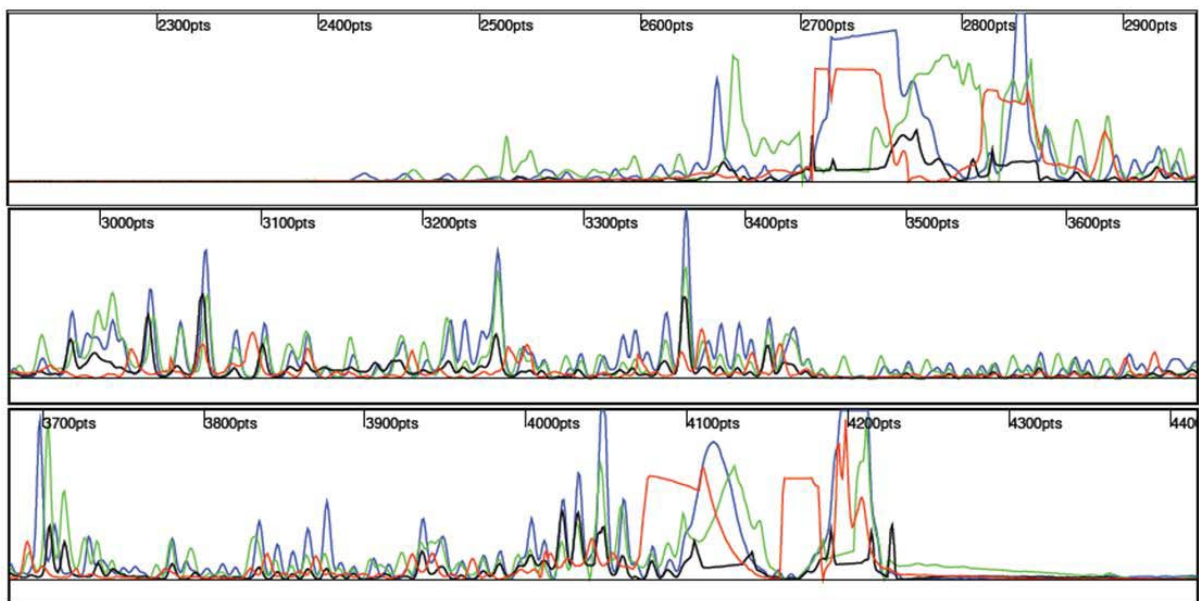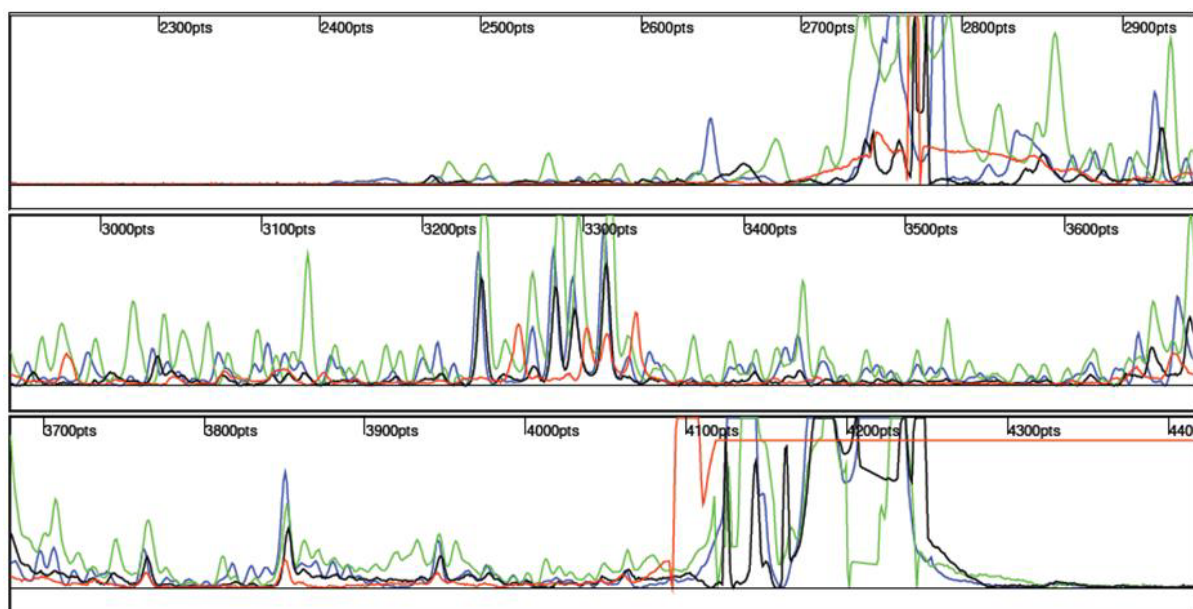
Figure 29. SHAPE data for the 5'UTR of the mouse APP mRNA transcript. The raw output from the ABI 310 genetic analyzer underwent baseline adjustment, matrixing, and mobility shift adjustment. Fluorescence-labeled DNA primer was annealed to the 3'-end of this 147-nucleotide RNA. The blue trace is the +1M7 sample; the black trace is the -1M7 negative control; green and red traces are two dideoxy ladders (ddG and ddA, respectively). The x-axis indicates the number of data points collected. The y-axis (not shown) enumerates the fluorescence units.
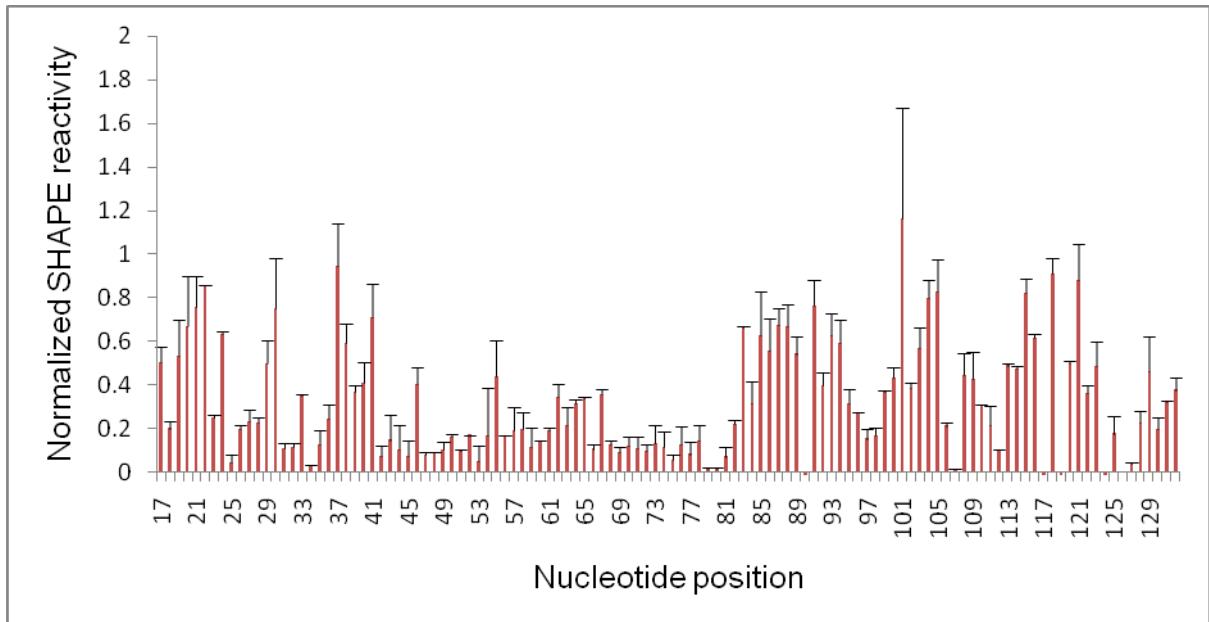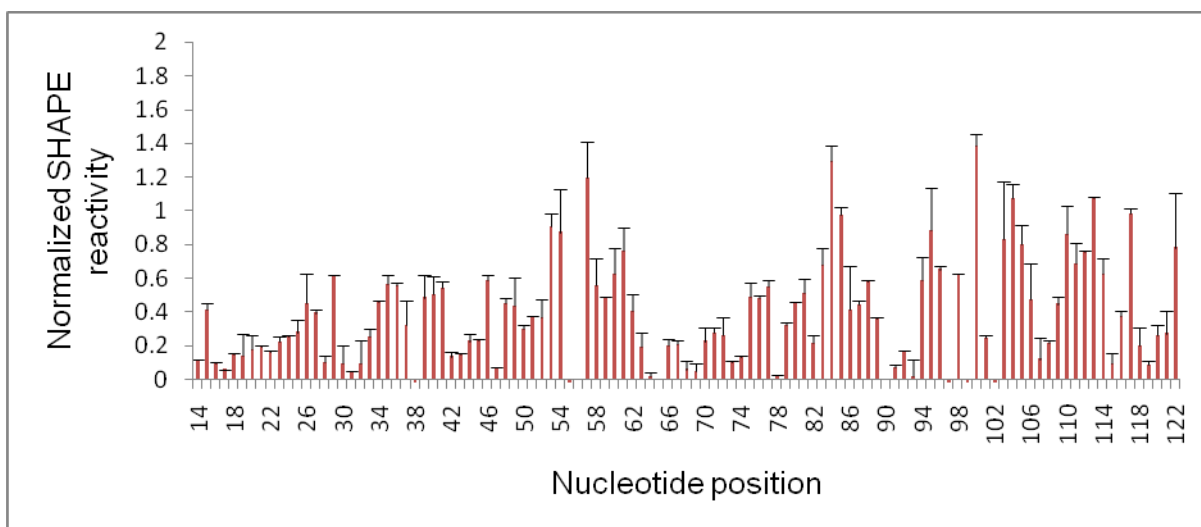
Figure 30. Single nucleotide resolution of normalized SHAPE reactivities for the mouse APP mRNA 5' UTR. Error bars represent standard deviations calculated from two independent experiments.
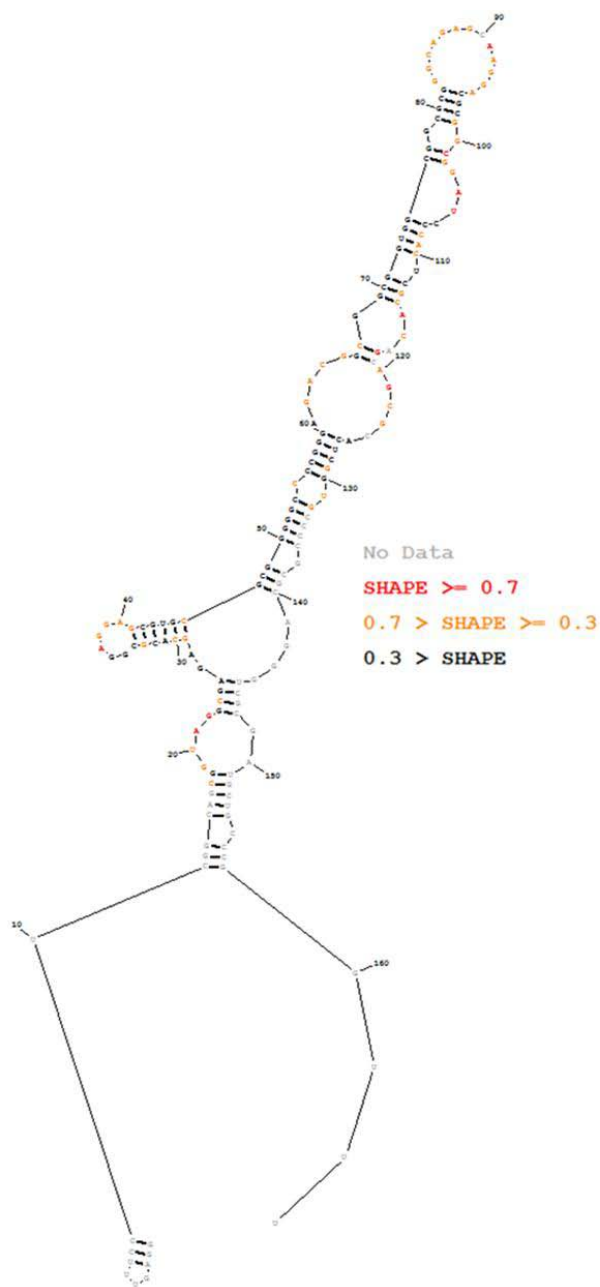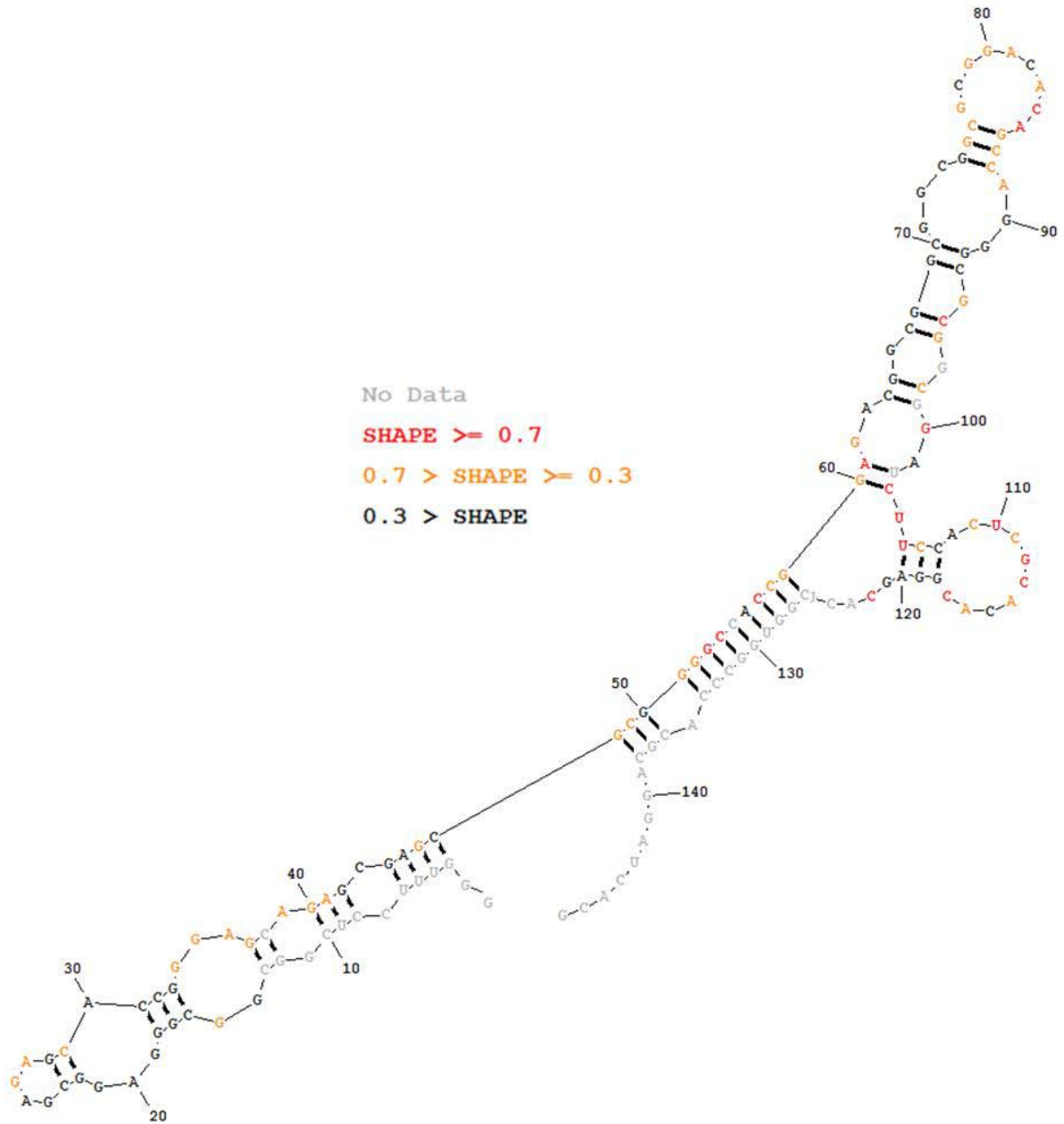
Figure 31. The predicted secondary structure of the 5'UTR of the mouse APP mRNA transcript. Nucleotides ar e co lored black (unreactive, SHAPE r eactivity <0.3), orange (moderately reactive, $0.3 \leq$ SHAPE reactivity <0.7), red (highly reactive, SHAPE reactivity $\geq$0.7), or grey (no data).

CHAPTER 4

__Discussion__

The AFM study of RNA conformation was not very successful. The length of the seven RNA transcripts investigated was between 140-240 nucleotides. Due to the relatively short length of the RNA molecules and their complex three-dimensional folding, AFM imaging only shows them as blobs. The difference in volume and height of the blobs representing these RNA molecules is somewhat random (see Table 1); no correlation has been observed between volume or height and RNA sequence length in this study. The day-to-day variation of the AFM instrument and tip conditions are considered to be important factors relative to these results.

In addition to the differences between RNA molecules of different types, the volume and height of the blobs for the same RNA molecule deposited onto the same mica surface show large variations (see standard deviations, SD, in Table 1). There are several possible explanations for the differences in height and volume of the blobs for the same RNA molecule, including 1) some blobs on the mica surface were RNA aggregates; 2) some blobs were degraded RNA molecules; and 3) the RNA molecules adopted different conformations on the mica surface. Overall, this study shows that AFM imaging is not an efficient way to visualize relatively short RNA molecules unless there are some distinct features present. For example, Jaeger's research group visualized the dimerization of a 230-nucleotide RNA

molecule via "kissing-loop" interaction; the AFM images showed double or triple blobs

caused by these "kissing-loop" structures.[75]

Table 1. Summary of the averaged height and volume of the blobs in AFM images

for each RNA molecule investigated ("nts" = nucleotides).

RNA	Human Ferritin-H mRNA 5'UTR (237 nts)	Human Ferritin-H mRNA short 5'UTR (207 nts)	Mouse Ferritin-H mRNA 5'UTR (169 nts)	Human Ferritin-L mRNA 5'UTR (217 nts)	Mouse Ferritin-L mRNA 5' UTR (207 nts)	Human APP mRNA 5'UTR (163 nts)	Mouse APP mRNA 5'UTR (147 nts)
Height of the blob in nm (Average ± SD)	0.33±0.20	0.65±0.26	0.53±0.16	1.01±0.26	0.83±0.14	0.37±0.03	2.56±0.41
Volume of the blob in nm^3 (Average ± SD)	356±360	1162±732	738±265	2316±1481	928±247	477±69	1722±609

SHAPE chemistry was used to map the secondary structures of the seven RNA

transcripts at single nucleotide resolution. To our knowledge, this is the first time that the

secondary structures of the 5'UTRs of APP mRNA from human and mouse have been

experimentally mapped. Several research groups have used traditional X-ray crystallization

techniques or enzymatic cleavage and/or chemical modification approaches to determine the

conformation of the IRE region (30-50 nucleotides) in the Ferritin-H and Ferritin-L mRNA

5'UTR, in the presence and absence of small molecule or protein ligands, but none of them

determined the structure of the entire 5'UTR of these RNA molecules.[85,86,88-91] This study

paves the way for the further investigation of RNA-ligand interactions in the 5'UTR of IRE-

containing mRNAs.

The seven RNA molecules show a high degree of secondary structure, with numerous

stem-loops structures. The Human Ferritin-H mRNA short 5'UTR, mouse Ferritin-H mRNA

5'UTR, human Ferritin-L mRNA 5'UTR, and mouse Ferritin-L mRNA 5'UTR form the

expected IRE stem-loop structure, which includes a CAGUGN apical loop (N can be A, C, or

U, but not G). The first nucleotide C pairs with the fifth nucleotide G within the loop for

efficient IRP protein binding. In addition to the apical loop, these IRE structures in the

5'UTR of the Ferritin mRNAs also contain a conserved 5-base-pair stem, followed by a

UGC-C type of bulge. The G-C base pair in the bulge is required for IRP binding.

The APP mRNA 5'UTR in human and mouse contains an IRE stem-loop structure

that is different from the IREs in the 5'UTRs of the Ferritin-H and Ferritin-L mRNAs.

Instead of having a 6-nucleotide apical loop comprised of CAGUGN, where N can be A, C,

or U, but not G, the human APP IRE contains a 13-nucleotide loop comprised of the

nucleotides GGCAGAGCAAGGA. The mouse APP IRE contains a 9-nucleotide apical loop

comprised of the nucleotides GCGGACACA. The human APP IRE contains a 4-base-pair

stem, followed by a G-G bulge. The mouse APP IRE contains a 3-base-pair stem, followed

by a 6-nucleotide internal loop.

In addition to the IRE stem-loop, the 5'UTR of the Ferritin-H, Ferritin-L, and APP mRNAs also contain an IL-1β-dependent acute box.[92-95] The acute boxes in the Ferritin mRNA 5'UTRs are located at the 3'-end of the 5'UTR. For example, the core region of the acute box in the human Ferritin-H mRNA 5'UTR includes nucleotides 191CGCCGCGCAGCCACCGCCGCCGCCG215, where little structural information was obtained. This occurred because the fluorescently labeled DNA primer was annealed to the 3'-end of the RNA molecule for the SHAPE procedure. During primer extension, the large primer peaks mask the structural information of the neighboring (i.e., the 3'-end) nucleotides.

The core region of the acute box in the human Ferritin-L mRNA 5'UTR is located at nucleotides U111 through G136, which contains a single-stranded region and a stem-loop structure. The core region of the acute box in the human APP mRNA 5'UTR is located at positions 101-125, where most nucleotides are reactive.

The SHAPE technique was successfully used to map the secondary structures of the seven RNA molecules in the absence of the ligand. The next step of our study is to determine the secondary structures of the RNA molecules in the presence of different ligands at various concentrations. A slab gel electrophoresis system will be used instead of capillary gel electrophoresis to separate and size radio-labeled cDNAs. This will allow us to run 20-30 SHAPE reactions in parallel on one gel, and to visualize the gradual structural transition undergone by the RNA. The transition mid-point will be determined and the ligand binding site will be predicted.

CHAPTER 5

Conclusions

In order to substantially improve the understanding of ligand-RNA binding mechanisms and to shed light on the design of novel molecules targeted to specific RNA motifs, a complete elucidation of the RNA conformation before, during, and after ligand binding is necessary. Tens of thousands of compounds have been screened to identify ligands that can bind to the 5'UTR of the human APP mRNA, which would allow the treatment of Alzheimer's disease by decreasing the production of APP and the corresponding Aβ; fifteen compounds were identified as inhibiting APP translation by interacting with the 5'UTR of APP mRNA, which includes an IRE stem-loop structure. However, the underlying mechanism(s) of these RNA-ligand interactions has not been determined. For example, what conformation does APP mRNA 5'UTR adopt after the binding of a small molecule? Which nucleotides do the ligands bind to in the IRE? Do the ligands also bind to other regions in the 5'UTR of the human APP mRNA, such as the interleukin-1-responsive acute box? If the molecules mentioned above have the capability to reduce APP expression, can they bind to the IRE region in the 5'UTR of the human Ferritin-H and Ferritin-L mRNA to inhibit the translation of these intracellular iron storage proteins as well? It is an advantage if the ligands can down-regulate APP expression, but certainly a disadvantage if they down-regulate the expression of ferritin.

The objective of this study was to determine the conformations of the 5'UTRs of Ferritin-H, Ferritin-L, and APP mRNA transcripts from two species (human and mouse) in the absence of the ligand. We used AFM to visualize the conformation of these RNA molecules, and determined the secondary RNA structures using SHAPE analysis coupled with a fluorescence detection system. To our knowledge, this is the first time that the secondary structures of the 5'UTRs of APP mRNA in human and mouse have been experimentally mapped. The AFM imaging did not provide high resolution structural information about these RNAs, whereas the SHAPE procedure successfully interrogated the secondary RNA structures at single nucleotide resolution. This study paves the way for the further investigation of RNA-ligand interactions in these RNA molecules.

References

1. Pelizzoni, I., Macco, R., Zacchetti, D., Grohovaz, F. & Codazzi, F. Iron and calcium in the central nervous system: a close relationship in health and sickness. *Biochem Soc Trans* **36**, 1309-1312 (2008).
2. Rogers, J.T., Bush, A.I., Cho, H.H., Smith, D.H., Thomson, A.M., Friedlich, A.L., Lahiri, D.K., Leedman, P.J., Huang, X. & Cahill, C.M. Iron and the translation of the amyloid precursor protein (APP) and ferritin mRNAs: riboregulation against neural oxidative damage in Alzheimer's disease. *Biochem Soc Trans* **36**, 1282-1287 (2008).
3. Munoz, M., Villar, I. & Garcia-Erce, J.A. An update on iron physiology. *World J Gastroenterol* **15**, 4617-4626 (2009).
4. Arosio, P., Ingrassia, R. & Cavadini, P. Ferritins: a family of molecules for iron storage, antioxidation and more. *Biochim Biophys Acta* **1790**, 589-599 (2009).
5. Dorner, M.H., Salfeld, J., Will, H., Leibold, E.A., Vass, J.K. & Munro, H.N. Structure of human ferritin light subunit messenger RNA: comparison with heavy subunit message and functional implications. *Proc Natl Acad Sci U S A* **82**, 3139-3143 (1985).
6. Theil, E.C. Ferritin: at the crossroads of iron and oxygen metabolism. *J Nutr* **133**, 1549S-1553S (2003).
7. Liu, X. & Theil, E.C. Ferritins: dynamic management of biological iron and oxygen chemistry. *Acc Chem Res* **38**, 167-175 (2005).
8. Kanter, M. Free radicals, exercise and antioxidant supplementation. *Proc Nutr Soc* **57**, 9-13 (1998).
9. Zablocka, A. & Janusz, M. [The two faces of reactive oxygen species]. *Postepy Hig Med Dosw (Online)* **62**, 118-124 (2008).
10. Thomson, A.M., Rogers, J.T. & Leedman, P.J. Iron-regulatory proteins, iron-responsive elements and ferritin mRNA translation. *Int J Biochem Cell Biol* **31**, 1139-1152 (1999).
11. Butt, J., Kim, H.Y., Basilion, J.P., Cohen, S., Iwai, K., Philpott, C.C., Altschul, S., Klausner, R.D. & Rouault, T.A. Differences in the RNA binding sites of iron regulatory proteins and potential target diversity. *Proc Natl Acad Sci U S A* **93**, 4345-4349 (1996).
12. Piccinelli, P. & Samuelsson, T. Evolution of the iron-responsive element. *RNA* **13**, 952-966 (2007).
13. Griffiths, P.D., Dobson, B.R., Jones, G.R. & Clarke, D.T. Iron in the basal ganglia in Parkinson's disease. An in vitro study using extended X-ray absorption fine structure and cryo-electron microscopy. *Brain* **122 (Pt 4)**, 667-673 (1999).
14. Berg, D., Gerlach, M., Youdim, M.B., Double, K.L., Zecca, L., Riederer, P. & Becker, G. Brain iron pathways and their relevance to Parkinson's disease. *J Neurochem* **79**, 225-236 (2001).
15. Bishop, G.M., Robinson, S.R., Liu, Q., Perry, G., Atwood, C.S. & Smith, M.A. Iron: a pathological mediator of Alzheimer disease? *Dev Neurosci* **24**, 184-187 (2002).
16. Sadrzadeh, S.M. & Saffari, Y. Iron and brain disorders. *Am J Clin Pathol* **121 Suppl**, S64-70 (2004).
17. Ong, W.Y. & Farooqui, A.A. Iron, neuroinflammation, and Alzheimer's disease. *J Alzheimers Dis* **8**, 183-200; discussion 209-115 (2005).

18.   Rouault, T.A. & Cooperman, S. Brain iron metabolism. *Semin Pediatr Neurol* **13**, 142-148 (2006).

19.   Altamura, S. & Muckenthaler, M.U. Iron toxicity in diseases of aging: Alzheimer's disease, Parkinson's disease and atherosclerosis. *J Alzheimers Dis* **16**, 879-895 (2009).

20.   Heron, M., Hoyert, D.L., Murphy, S.L., Xu, J., Kochanek, K.D. & Tejada-Vera, B. Deaths: final data for 2006. *Natl Vital Stat Rep* **57**, 1-134 (2009).

21.   Alzheimer, A., Stelzmann, R.A., Schnitzlein, H.N. & Murtagh, F.R. An English translation of Alzheimer's 1907 paper, "Uber eine eigenartige Erkankung der Hirnrinde". *Clin Anat* **8**, 429-431 (1995).

22.   Bennett, D.A. Alzheimer's disease--introduction. *Dis Mon* **46**, 653-656 (2000).

23.   2009 Alzheimer's disease facts and figures. *Alzheimers Dement* **5**, 234-270 (2009).

24.   Glabe, C. Biomedicine. Avoiding collateral damage in Alzheimer's disease treatment. *Science* **314**, 602-603 (2006).

25.   Selkoe, D.J., Yamazaki, T., Citron, M., Podlisny, M.B., Koo, E.H., Teplow, D.B. & Haass, C. The role of APP processing and trafficking pathways in the formation of amyloid beta-protein. *Ann N Y Acad Sci* **777**, 57-64 (1996).

26.   Nunan, J. & Small, D.H. Regulation of APP cleavage by alpha-, beta- and gamma-secretases. *FEBS Lett* **483**, 6-10 (2000).

27.   Kume, H., Sekijima, Y., Maruyama, K. & Kametani, F. gamma-Secretase can cleave amyloid precursor protein fragments independent of alpha- and beta-secretase pre-cutting. *Int J Mol Med* **12**, 57-60 (2003).

28.   Steiner, H. Uncovering gamma-secretase. *Curr Alzheimer Res* **1**, 175-181 (2004).

29.   Small, D.H., Mok, S.S. & Bornstein, J.C. Alzheimer's disease and Abeta toxicity: from top to bottom. *Nat Rev Neurosci* **2**, 595-598 (2001).

30.   Li, Y., Zhou, W., Tong, Y., He, G. & Song, W. Control of APP processing and Abeta generation level by BACE1 enzymatic activity and transcription. *FASEB J* **20**, 285-292 (2006).

31.   Lammich, S., Schobel, S., Zimmer, A.K., Lichtenthaler, S.F. & Haass, C. Expression of the Alzheimer protease BACE1 is suppressed via its 5'-untranslated region. *EMBO Rep* **5**, 620-625 (2004).

32.   Willem, M., Lammich, S. & Haass, C. Function, regulation and therapeutic properties of beta-secretase (BACE1). *Semin Cell Dev Biol* **20**, 175-182 (2009).

33.   Yang, L.B., Lindholm, K., Yan, R., Citron, M., Xia, W., Yang, X.L., Beach, T., Sue, L., Wong, P., Price, D., Li, R. & Shen, Y. Elevated beta-secretase expression and enzymatic activity detected in sporadic Alzheimer disease. *Nat Med* **9**, 3-4 (2003).

34.   Li, R., Lindholm, K., Yang, L.B., Yue, X., Citron, M., Yan, R., Beach, T., Sue, L., Sabbagh, M., Cai, H., Wong, P., Price, D. & Shen, Y. Amyloid beta peptide load is correlated with increased beta-secretase activity in sporadic Alzheimer's disease patients. *Proc Natl Acad Sci U S A* **101**, 3632-3637 (2004).

35.   Tesco, G., Koh, Y.H., Kang, E.L., Cameron, A.N., Das, S., Sena-Esteves, M., Hiltunen, M., Yang, S.H., Zhong, Z., Shen, Y., Simpkins, J.W. & Tanzi, R.E. Depletion of GGA3 stabilizes BACE and enhances beta-secretase activity. *Neuron* **54**, 721-737 (2007).

36. Zacchetti, D., Chieregatti, E., Bettegazzi, B., Mihailovich, M., Sousa, V.L., Grohovaz, F. & Meldolesi, J. BACE1 expression and activity: relevance in Alzheimer's disease. *Neurodegener Dis* **4**, 117-126 (2007).

37. Fukumoto, H., Cheung, B.S., Hyman, B.T. & Irizarry, M.C. Beta-secretase protein and activity are increased in the neocortex in Alzheimer disease. *Arch Neurol* **59**, 1381-1389 (2002).

38. Castellani, R.J., Moreira, P.I., Liu, G., Dobson, J., Perry, G., Smith, M.A. & Zhu, X. Iron: the Redox-active center of oxidative stress in Alzheimer disease. *Neurochem Res* **32**, 1640-1645 (2007).

39. Smith, M.A., Harris, P.L., Sayre, L.M. & Perry, G. Iron accumulation in Alzheimer disease is a source of redox-generated free radicals. *Proc Natl Acad Sci U S A* **94**, 9866-9868 (1997).

40. Smith, M.A. & Perry, G. Free radical damage, iron, and Alzheimer's disease. *J Neurol Sci* **134 Suppl**, 92-94 (1995).

41. Brar, S., Henderson, D., Schenck, J. & Zimmerman, E.A. Iron accumulation in the substantia nigra of patients with Alzheimer disease and parkinsonism. *Arch Neurol* **66**, 371-374 (2009).

42. Grundke-Iqbal, I., Fleming, J., Tung, Y.C., Lassmann, H., Iqbal, K. & Joshi, J.G. Ferritin is a component of the neuritic (senile) plaque in Alzheimer dementia. *Acta Neuropathol* **81**, 105-110 (1990).

43. Parkinson, J. An essay on the shaking palsy. 1817. *J Neuropsychiatry Clin Neurosci* **14**, 223-236; discussion 222 (2002).

44. Bradbury, J. Alpha-synuclein gene triplication discovered in Parkinson's disease. *Lancet Neurol* **2**, 715 (2003).

45. Singleton, A.B., Farrer, M., Johnson, J., Singleton, A., Hague, S., Kachergus, J., Hulihan, M., Peuralinna, T., Dutra, A., Nussbaum, R., Lincoln, S., Crawley, A., Hanson, M., Maraganore, D., Adler, C., Cookson, M.R., Muenter, M., Baptista, M., Miller, D., Blancato, J., Hardy, J. & Gwinn-Hardy, K. alpha-Synuclein locus triplication causes Parkinson's disease. *Science* **302**, 841 (2003).

46. Chartier-Harlin, M.C., Kachergus, J., Roumier, C., Mouroux, V., Douay, X., Lincoln, S., Levecque, C., Larvor, L., Andrieux, J., Hulihan, M., Waucquier, N., Defebvre, L., Amouyel, P., Farrer, M. & Destee, A. Alpha-synuclein locus duplication as a cause of familial Parkinson's disease. *Lancet* **364**, 1167-1169 (2004).

47. Miller, D.W., Hague, S.M., Clarimon, J., Baptista, M., Gwinn-Hardy, K., Cookson, M.R. & Singleton, A.B. Alpha-synuclein in blood and brain from familial Parkinson disease with SNCA locus triplication. *Neurology* **62**, 1835-1838 (2004).

48. Zarranz, J.J., Alegre, J., Gomez-Esteban, J.C., Lezcano, E., Ros, R., Ampuero, I., Vidal, L., Hoenicka, J., Rodriguez, O., Atares, B., Llorens, V., Gomez Tortosa, E., del Ser, T., Munoz, D.G. & de Yebenes, J.G. The new mutation, E46K, of alpha-synuclein causes Parkinson and Lewy body dementia. *Ann Neurol* **55**, 164-173 (2004).

49. Tan, E.K., Chandran, V.R., Fook-Chong, S., Shen, H., Yew, K., Teoh, M.L., Yuen, Y. & Zhao, Y. Alpha-synuclein mRNA expression in sporadic Parkinson's disease. *Mov Disord* **20**, 620-623 (2005).

50. Schapira, A.H. Pathogenesis of Parkinson's disease. *Baillieres Clin Neurol* **6**, 15-36 (1997).

51.   Pals, P., Lincoln, S., Manning, J., Heckman, M., Skipper, L., Hulihan, M., Van den Broeck, M., De Pooter, T., Cras, P., Crook, J., Van Broeckhoven, C. & Farrer, M.J. alpha-Synuclein promoter confers susceptibility to Parkinson's disease. *Ann Neurol* **56**, 591-595 (2004).

52.   Gorell, J.M., Ordidge, R.J., Brown, G.G., Deniau, J.C., Buderer, N.M. & Helpern, J.A. Increased iron-related MRI contrast in the substantia nigra in Parkinson's disease. *Neurology* **45**, 1138-1143 (1995).

53.   Becker, G., Muller, A., Braune, S., Buttner, T., Benecke, R., Greulich, W., Klein, W., Mark, G., Rieke, J. & Thumler, R. Early diagnosis of Parkinson's disease. *J Neurol* **249 Suppl 3**, III/40-48 (2002).

54.   Faucheux, B.A., Martin, M.E., Beaumont, C., Hunot, S., Hauw, J.J., Agid, Y. & Hirsch, E.C. Lack of up-regulation of ferritin is associated with sustained iron regulatory protein-1 binding activity in the substantia nigra of patients with Parkinson's disease. *J Neurochem* **83**, 320-330 (2002).

55.   Rogers, J.T., Randall, J.D., Cahill, C.M., Eder, P.S., Huang, X., Gunshin, H., Leiter, L., McPhee, J., Sarang, S.S., Utsuki, T., Greig, N.H., Lahiri, D.K., Tanzi, R.E., Bush, A.I., Giordano, T. & Gullans, S.R. An iron-responsive element type II in the 5'-untranslated region of the Alzheimer's amyloid precursor protein transcript. *J Biol Chem* **277**, 45518-45528 (2002).

56.   Friedlich, A.L., Tanzi, R.E. & Rogers, J.T. The 5'-untranslated region of Parkinson's disease alpha-synuclein messengerRNA contains a predicted iron responsive element. *Mol Psychiatry* **12**, 222-223 (2007).

57.   Olivares, D., Huang, X., Branden, L., Greig, N.H. & Rogers, J.T. Physiological and Pathological Role of Alpha-synuclein in Parkinson's Disease Through Iron Mediated Oxidative Stress; The Role of a Putative Iron-responsive Element. *Int J Mol Sci* **10**, 1226-1260 (2009).

58.   Cahill, C.M., Lahiri, D.K., Huang, X. & Rogers, J.T. Amyloid precursor protein and alpha synuclein translation, implications for iron and inflammation in neurodegenerative diseases. *Biochim Biophys Acta* **1790**, 615-628 (2009).

59.   Rogers, J.T., Randall, J.D., Eder, P.S., Huang, X., Bush, A.I., Tanzi, R.E., Venti, A., Payton, S.M., Giordano, T., Nagano, S., Cahill, C.M., Moir, R., Lahiri, D.K., Greig, N., Sarang, S.S. & Gullans, S.R. Alzheimer's disease drug discovery targeted to the APP mRNA 5'untranslated region. *J Mol Neurosci* **19**, 77-82 (2002).

60.   Payton, S., Cahill, C.M., Randall, J.D., Gullans, S.R. & Rogers, J.T. Drug discovery targeted to the Alzheimer's APP mRNA 5'-untranslated region: the action of paroxetine and dimercaptopropanol. *J Mol Neurosci* **20**, 267-275 (2003).

61.   Reznichenko, L., Amit, T., Zheng, H., Avramovich-Tirosh, Y., Youdim, M.B., Weinreb, O. & Mandel, S. Reduction of iron-regulated amyloid precursor protein and beta-amyloid peptide by (-)-epigallocatechin-3-gallate in cell cultures: implications for iron chelation in Alzheimer's disease. *J Neurochem* **97**, 527-536 (2006).

62.   Mandel, S., Weinreb, O., Reznichenko, L., Kalfon, L. & Amit, T. Green tea catechins as brain-permeable, non toxic iron chelators to "iron out iron" from the brain. *J Neural Transm Suppl*, 249-257 (2006).

63.   Bandyopadhyay, S., Ni, J., Ruggiero, A., Walshe, K., Rogers, M.S., Chattopadhyay, N., Glicksman, M.A. & Rogers, J.T. A high-throughput drug screen targeted to the

5'untranslated region of Alzheimer amyloid precursor protein mRNA. *J Biomol Screen* **11**, 469-480 (2006).

64. Utsuki, T., Yu, Q.S., Davidson, D., Chen, D., Holloway, H.W., Brossi, A., Sambamurti, K., Lahiri, D.K., Greig, N.H. & Giordano, T. Identification of novel small molecule inhibitors of amyloid precursor protein synthesis as a route to lower Alzheimer's disease amyloid-beta peptide. *J Pharmacol Exp Ther* **318**, 855-862 (2006).

65. Zheng, H., Gal, S., Weiner, L.M., Bar-Am, O., Warshawsky, A., Fridkin, M. & Youdim, M.B. Novel multifunctional neuroprotective iron chelator-monoamine oxidase inhibitor drugs for neurodegenerative diseases: in vitro studies on antioxidant activity, prevention of lipid peroxide formation and monoamine oxidase inhibition. *J Neurochem* **95**, 68-78 (2005).

66. Kupershmidt, L., Weinreb, O., Amit, T., Mandel, S., Carri, M.T. & Youdim, M.B. Neuroprotective and neuritogenic activities of novel multimodal iron-chelating drugs in motor-neuron-like NSC-34 cells and transgenic mouse model of amyotrophic lateral sclerosis. *FASEB J* **23**, 3766-3779 (2009).

67. Binnig, G., Quate, C.F. & Gerber, C. Atomic force microscope. *Phys Rev Lett* **56**, 930-933 (1986).

68. Gadegaard, N. Atomic force microscopy in biology: technology and techniques. *Biotech Histochem* **81**, 87-97 (2006).

69. Czajkowsky, D.M., Iwamoto, H. & Shao, Z. Atomic force microscopy in structural biology: from the subcellular to the submolecular. *J Electron Microsc (Tokyo)* **49**, 395-406 (2000).

70. Lyubchenko, Y.L., Jacobs, B.L., Lindsay, S.M. & Stasiak, A. Atomic force microscopy of nucleoprotein complexes. *Scanning Microsc* **9**, 705-724; discussion 724-707 (1995).

71. Engel, A. & Muller, D.J. Observing single biomolecules at work with the atomic force microscope. *Nat Struct Biol* **7**, 715-718 (2000).

72. Bustamante, C., Rivetti, C. & Keller, D.J. Scanning force microscopy under aqueous solutions. *Curr Opin Struct Biol* **7**, 709-716 (1997).

73. Yang, J. & Shao, Z. Recent advances in biological atomic force microscopy. *Micron* **26**, 35-49 (1995).

74. Hansma, H.G., Kasuya, K. & Oroudjev, E. Atomic force microscopy imaging and pulling of nucleic acids. *Curr Opin Struct Biol* **14**, 380-385 (2004).

75. Hansma, H.G., Oroudjev, E., Baudrey, S. & Jaeger, L. TectoRNA and 'kissing-loop' RNA: atomic force microscopy of self-assembling RNA structures. *J Microsc* **212**, 273-279 (2003).

76. Giro, A., Bergia, A., Zuccheri, G., Bink, H.H., Pleij, C.W. & Samori, B. Single molecule studies of RNA secondary structure: AFM of TYMV viral RNA. *Microsc Res Tech* **65**, 235-245 (2004).

77. Alvarez, D.E., Lodeiro, M.F., Luduena, S.J., Pietrasanta, L.I. & Gamarnik, A.V. Long-range RNA-RNA interactions circularize the dengue virus genome. *J Virol* **79**, 6631-6643 (2005).

78. Merino, E.J., Wilkinson, K.A., Coughlan, J.L. & Weeks, K.M. RNA structure analysis at single nucleotide resolution by selective 2'-hydroxyl acylation and primer extension (SHAPE). *J Am Chem Soc* **127**, 4223-4231 (2005).

79. Wilkinson, K.A., Merino, E.J. & Weeks, K.M. RNA SHAPE chemistry reveals nonhierarchical interactions dominate equilibrium structural transitions in tRNA(Asp) transcripts. *J Am Chem Soc* **127**, 4659-4667 (2005).

80. Mortimer, S.A. & Weeks, K.M. A fast-acting reagent for accurate analysis of RNA secondary and tertiary structure by SHAPE chemistry. *J Am Chem Soc* **129**, 4144-4145 (2007).

81. Wang, B., Wilkinson, K.A. & Weeks, K.M. Complex ligand-induced conformational changes in tRNA(Asp) revealed by single-nucleotide resolution SHAPE chemistry. *Biochemistry* **47**, 3454-3461 (2008).

82. Wilkinson, K.A., Gorelick, R.J., Vasa, S.M., Guex, N., Rein, A., Mathews, D.H., Giddings, M.C. & Weeks, K.M. High-throughput SHAPE analysis reveals structures in HIV-1 genomic RNA strongly conserved across distinct biological states. *PLoS Biol* **6**, e96 (2008).

83. Vasa, S.M., Guex, N., Wilkinson, K.A., Weeks, K.M. & Giddings, M.C. ShapeFinder: a software system for high-throughput quantitative analysis of nucleic acid reactivity information resolved by capillary electrophoresis. *RNA* **14**, 1979-1990 (2008).

84. Mathews, D.H., Disney, M.D., Childs, J.L., Schroeder, S.J., Zuker, M. & Turner, D.H. Incorporating chemical modification constraints into a dynamic programming algorithm for prediction of RNA secondary structure. *Proc Natl Acad Sci U S A* **101**, 7287-7292 (2004).

85. Selezneva, A.I., Cavigiolio, G., Theil, E.C., Walden, W.E. & Volz, K. Crystallization and preliminary X-ray diffraction analysis of iron regulatory protein 1 in complex with ferritin IRE RNA. *Acta Crystallogr Sect F Struct Biol Cryst Commun* **62**, 249-252 (2006).

86. Walden, W.E., Selezneva, A.I., Dupuy, J., Volbeda, A., Fontecilla-Camps, J.C., Theil, E.C. & Volz, K. Structure of dual function iron regulatory protein 1 complexed with ferritin IRE-RNA. *Science* **314**, 1903-1908 (2006).

87. Maloney, B., Ge, Y.W., Greig, N. & Lahiri, D.K. Presence of a "CAGA box" in the APP gene unique to amyloid plaque-forming species and absent in all APLP-1/2 genes: implications in Alzheimer's disease. *FASEB J* **18**, 1288-1290 (2004).

88. Harrell, C.M., McKenzie, A.R., Patino, M.M., Walden, W.E. & Theil, E.C. Ferritin mRNA: interactions of iron regulatory element with translational regulator protein P-90 and the effect on base-paired flanking regions. *Proc Natl Acad Sci U S A* **88**, 4166-4170 (1991).

89. Wang, Y.H., Lin, P.N., Sczekan, S.R., McKenzie, R.A. & Theil, E.C. Ferritin mRNA probed, near the iron regulatory region, with protein and chemical (1,10-phenanthroline-Cu) nucleases. A possible role for base-paired flanking regions. *Biol Met* **4**, 56-61 (1991).

90. Canzoneri, J.C. & Oyelere, A.K. Interaction of anthracyclines with iron responsive element mRNAs. *Nucleic Acids Res* **36**, 6825-6834 (2008).

91. Tibodeau, J.D., Fox, P.M., Ropp, P.A., Theil, E.C. & Thorp, H.H. The up-regulation of ferritin expression using a small-molecule ligand to the native mRNA. *Proc Natl Acad Sci U S A* **103**, 253-257 (2006).

92. Rogers, J.T., Andriotakis, J.L., Lacroix, L., Durmowicz, G.P., Kasschau, K.D. & Bridges, K.R. Translational enhancement of H-ferritin mRNA by interleukin-1 beta

acts through 5' leader sequences distinct from the iron responsive element. *Nucleic Acids Res* **22**, 2678-2686 (1994).

93.   Rogers, J.T. Ferritin translation by interleukin-1and interleukin-6: the role of sequences upstream of the start codons of the heavy and light subunit genes. *Blood* **87**, 2525-2537 (1996).

94.   Rogers, J.T., Leiter, L.M., McPhee, J., Cahill, C.M., Zhan, S.S., Potter, H. & Nilsson, L.N. Translation of the alzheimer amyloid precursor protein mRNA is up-regulated by interleukin-1 through 5'-untranslated region sequences. *J Biol Chem* **274**, 6421-6431 (1999).

95.   Thomson, A.M., Cahill, C.M., Cho, H.H., Kassachau, K.D., Epis, M.R., Bridges, K.R., Leedman, P.J. & Rogers, J.T. The acute box cis-element in human heavy ferritin mRNA 5'-untranslated region is a unique translation enhancer that binds poly(C)-binding proteins. *J Biol Chem* **280**, 30032-30045 (2005).